



# Discrete Element Study on the Effects of Geogrid Characteristics on the Mechanical Response of Reinforced Ballast Under Cyclic Loading

Romarc Léo Esteban Desbrousses<sup>1</sup> · Mohamed A. Meguid<sup>1</sup> · Sam Bhat<sup>2</sup>

Accepted: 6 May 2024

© The Author(s), under exclusive licence to Springer Science+Business Media, LLC, part of Springer Nature 2024

## Abstract

This study presents an investigation into the mechanical behavior of geogrid-reinforced ballast subjected to cyclic loading focusing on the macro- and micromechanical features of the geogrid-ballast interaction mechanism. Key areas of interest include the effects of geogrid placement depth, aperture size, and stiffness on the motion of ballast particles, formation of contact force chains, and energy dissipation. A three-dimensional discrete element model, calibrated with experimental data, simulates ballast box tests performed on 300-mm-thick ballast layers reinforced by geogrids placed at depths ranging from 50 to 250 mm below the tie. The findings reveal that geogrids located within the upper 150 mm of the ballast layer significantly reduce tie settlement by minimizing particle movement, creating well-connected soil structures, and decreasing energy dissipation. Upon identifying 150 mm as the optimal geogrid placement depth, a parametric study evaluates the impact of the geogrid aperture size ( $A$ ) and stiffness on the behavior of geogrid-reinforced ballast. The geogrid aperture size ( $A$ ) is varied to give aperture size to ballast diameter ( $D$ ) ratios ranging from 1.09 to 2.91, while the geogrid's stiffness ranges from 9.54 to 18.00 kN/m. Results indicate that  $A/D$  ratios greater than or equal to 1.45 are required for geogrids to perform satisfactorily, while stiffness appears to wield a negligible influence on the response of geogrid-reinforced ballast.

**Keywords** Reinforced ballast · Soft subgrade · Aperture size · Geogrid stiffness · Discrete element modeling

## Nomenclature

$\underline{A}$	Contact area between two contacting pieces or geogrid aperture size
$A$	Parallel bond cross-sectional area
$D_{50}$	Mean ballast particle diameter
$\Delta\delta_n$	Relative normal displacement increment
$\Delta\delta_s$	Adjusted relative shear displacement increment

Extended author information available on the last page of the article

$\Delta\delta_s^k$	Shear displacement's elastic component
$\Delta\delta_s^\mu$	Shear displacement's slip component
$E_m$	Mechanical energy
$E_{mb}$	Mechanical body energy
$E_{mc}$	Mechanical contact energy
$E_{pot}$	Potential energy
$E_{kin}$	Kinetic energy
$E_{damp}$	Energy dissipated by non-viscous damping
$E_k$	Strain energy stored in the linear springs
$\overline{E}_\mu$	Energy dissipated by frictional slip
$\overline{E}_k$	Strain energy stored in a geogrid's parallel bond springs
$\overline{E}^*$	Linear effective modulus
$\overline{E}_s^*$	Parallel bond effective modulus
$\varepsilon_1$	Major principal strain
$\varepsilon_3$	Minor principal strain
$F_c$	Contact force between contacting clumps
$F_n^l$	Linear normal force
$F^l$	Linear shear force
$\overline{F}_s$	Parallel-bond force
$\overline{F}_c$	Mean interparticle contact force
$\overline{F}_n$	Normal component of the parallel-bond force
$\overline{F}_s$	Shear component of the parallel-bond force
$\overline{g}_s$	Surface gap
$\overline{I}$	Parallel bond cross section's moment of inertia
$\overline{J}$	Parallel bond cross section's polar moment of inertia
$k_n$	Linear normal stiffness
$k_s$	Linear shear stiffness
$k_t$	Geogrid torsional stiffness
$\overline{k}_n$	Parallel bond normal stiffness
$\overline{k}_s$	Parallel bond shear stiffness
$\overline{\kappa}^*$	Linear normal-to-shear stiffness ratio
$\overline{\kappa}^*$	Parallel bond normal-to-shear stiffness ratio
$\kappa$	Deviatoric strain
$L$	Distance between the centroid of two contacting pieces
$\overline{M}_t$	Twisting moment
$\overline{M}$	Parallel-bond moment
$\overline{M}_t$	Twisting moment component of the parallel-bond moment
$\overline{M}_b$	Bending moment component of the parallel-bond moment
$N_c$	Number of contacts in a ballast layer
$N_p$	Number of particles in a ballast layer
$\mathbf{n}_c$	Unit vector defining the contact place
$\mu$	Friction coefficient
$p$	Hydrostatic stress invariant
$q$	Deviatoric stress invariant
$R$	Radius of a <i>PFC</i> ball

$\bar{R}$	The parallel bond's radius
$\sigma_d$	Deviator stress
$\sigma_{max}$	Maximum normal stress at the parallel-bond periphery
$\sigma_1$	Major principal stress
$\sigma_3$	Minor principal stress
$\tau_{max}$	Maximum shear stress at the parallel-bond periphery
$\theta_t$	aperture rotation

## 1 Introduction

Railroad tracks are generally supported by a ballasted substructure that includes a ballast layer, consisting of large, angular crushed rocks overlying a subballast layer resting on a subgrade (D. Li et al. 2015; Selig & Waters 1994). The ballast's primary functions include distributing the train loads to the underlying soil layers, maintaining track alignment, facilitating water drainage, and providing resilience against large dynamic train loads (Chen et al. 2022b; Dahlberg 2001; Desbrousses & Meguid 2021). However, owing to the unbound nature of its aggregate and its exposure to cyclic loading, the ballast layer is prone to experiencing substantial deformations and degradation of its particles (Indraratna et al. 2005; Malisetty et al. 2022; Thakur et al. 2013). This causes the ballast layer to be one of the main vectors of track settlement, which is one of the key challenges in railroad engineering due to its adverse effect on track geometry (D'Angelo et al. 2018; Desbrousses & Meguid 2022; Kumar et al. 2019; K. Wang et al. 2020).

As such, geogrids are increasingly used to mitigate deformations in ballast layers by leveraging their open structure to develop a robust mechanical interlock with the surrounding ballast particles, resulting in the formation of a semi-rigid mat that confines the ballast aggregate. The behavior of geogrid-reinforced ballast has been experimentally investigated through various test methods such as the direct shear test (Sadeghi et al. 2020; Sweta & Hussaini 2018,2019; Tutumluer et al. 2012), tri-axial test (Mishra et al. 2014; Qian et al. 2015, 2018; Yu et al. 2019), ballast box test (Desbrousses et al. 2023; Indraratna et al. 2013; S. Liu et al. 2016; Sadeghi et al. 2023), and field/full-scale tests (Esmaceli et al. 2017; Fernandes et al. 2008; Indraratna et al. 2010; Luo et al. 2023b). Experimental research has shown that the behavior of geogrid-reinforced ballast hinges on key geogrid characteristics such as the geogrid's placement depth, its aperture size, and its stiffness, as well as the strength of the underlying subgrade.

The placement depth of a geogrid within railroad ballast impacts the geogrid's ability to stabilize the unbound aggregate (Das 2016; Shin et al. 2002; Shin & Das 2000). Large-scale ballast box tests have demonstrated that geogrids placed closer to the bottom of the ties are more effective at reducing vertical and lateral ballast deformations compared to geogrids located deeper in the granular layer (Bathurst et al. 1986; Bathurst & Raymond 1987; Desbrousses et al. 2023; Indraratna et al. 2013). It is also typically recommended to place geogrids at least 150 mm beneath the ties to avoid interfering with ballast maintenance operations (Bathurst & Raymond

1987; Das 2016; Desbrousses & Meguid 2021). The geogrid aperture size has also been shown to be the backbone of the geogrid-ballast interlock and the corresponding increase in ballast shear strength (Mishra et al. 2014; Qian et al. 2015, 2018). Direct shear tests and ballast box tests performed on geogrid-reinforced ballast by Indraratna et al. (2012, 2013), Hussaini et al. (2015, 2016), and Sadeghi et al. (2020, 2023) revealed that optimal geogrid reinforcement is achieved when the ratio between the geogrid's aperture size ( $A$ ) and the ballast's mean particle diameter ( $D_{50}$ ) lies between 0.95 and 1.20. However, Brown et al. (2007) advocated for  $A/D_{50}$  ratios between 1.20 and 1.60 to maximize reductions in tie settlement. Experimental investigations on the effect of subgrade strength on the behavior of geogrid-reinforced ballast further highlighted that a geogrid's reinforcement effect is more pronounced over soft subgrades (Bathurst & Raymond 1987; Brown et al. 2007; Desbrousses et al. 2023, 2024; Desbrousses & Meguid 2022). Desbrousses et al. (2023, 2024) also noted that geogrids located closer to the bottom of the ties become more effective at stabilizing ballast as the subgrade strength decreases. Additionally, the stiffness of a geogrid embedded in ballast has been reported to impact its ability to reinforce the granular material, with Brown et al. (2007) and Jiang et al. (2019) showing that stiffer geogrids exhibit a greater propensity to reduce tie settlement compared to softer geogrids.

In a laboratory setting, analyzing the mechanical behavior of geogrid-reinforced ballast relies on observable macroscale processes, such as the evolution of tie settlement. However, experiments often fall short of capturing the intricate microscale interactions that occur within a geogrid-ballast system. To address this issue, researchers have turned to the discrete element method (DEM) to explore the behavior of geogrid-reinforced ballast from a particulate perspective. Pullout test simulations performed by McDowell et al. (2006), Ferellec and McDowell (2012), and Chen et al. (2013, 2014) on geogrids embedded in ballast shed light on the geogrid deformations that develop during pullout and highlighted the contribution of the geogrid-ballast interlock to pullout resistance by analyzing contact force chains. Direct shear test simulations performed by Ngo et al. (2014, 2016) showed that geogrids affect the formation of contact force chains during shearing in a ballast assembly and increase the number of interparticle contacts compared to an unreinforced ballast specimen. Gao and Meguid (2018) also reported that including geogrids in crushed rock aggregate minimizes particle rotation during bearing capacity tests and contributes to increasing the soil's bearing capacity. Similarly, Luo et al. (2023a, b) indicated that placing a geogrid at the ballast/subballast interface increases the ballast's coordination number, reduces particle rotation, decreases the mean interparticle contact force, and minimizes tie settlement. Other DEM studies investigated the effect of the geogrid aperture size on the geosynthetic's ability to reinforce ballast. Chen et al. (2023) recommended using geogrids with an aperture size of  $40 \times 40$  mm at the ballast/subballast interface to prevent the formation of ballast pockets. Additionally, Feng et al. (2023) and Wang et al. (2024) simulated direct shear tests on geogrid-reinforced unbound aggregate such as ballast and indicated that an  $A/D_{50}$  ratio of 2.53 leads to optimal geogrid performance based on analyses of contact force chains, energy dissipation, and particle movement. However, few studies have investigated the effect of key geogrid characteristics, such as a geogrid's

aperture size, stiffness, and placement depth, on the micromechanical behavior of a geogrid-reinforced ballast assembly subjected to cyclic loading.

Therefore, in this paper, a three-dimensional discrete element model is developed to simulate cyclic loading ballast box tests performed on a 300-mm-thick ballast layer and delve into the micromechanical causes of observable macroscopic phenomena such as tie settlement. The model's contact model parameters are calibrated using results from triaxial tests conducted on railroad ballast and geogrid tensile and aperture stability modulus tests. This study then explores the kinematics of ballast assemblies reinforced with geogrids positioned at varying depths ranging from 50 to 250 mm below the tie. The influence of the geogrid's aperture size ( $A$ ) and stiffness is then assessed by varying the geogrid aperture size to ballast diameter ratio ( $A/D$ ) from 1.09 to 2.91 and the geogrid's stiffness from 9.54 to 18.00 kN/m.

## 2 Overview of the Experimental Campaign

Desbrousses et al. (2023) performed a series of large-scale ballast box tests to investigate the effect of subgrade strength and geogrid placement depth on the deformation behavior of railroad ballast subjected to cyclic loading. In each experiment, a 300-mm-thick layer of railroad ballast was constructed in three 100-mm-thick lifts compacted to an approximate unit weight of  $15.7 \text{ kN/m}^3$  in a ballast box with plan dimensions of 1290 mm by 915 mm and a height of 600 mm. The ballast aggregate used in the experiments consisted of crushed granite aggregate screened to conform to an AREMA No. 4 gradation. Upon constructing the granular assembly, a model tie with plan dimensions of  $203 \times 301$  mm was placed above the compacted ballast layer. A cyclic compressive load with a mean value of 14 kN and an amplitude of 10.5 kN were applied to the tie at a frequency of 0.8 Hz following a sinusoidal waveform for a total of 40,000 repetitions using a pneumatic cyclic loading apparatus developed by Desbrousses and Meguid (2023b). The load delivered to the tie was monitored by a load cell mounted on the pneumatic cyclic loading apparatus, while the tie's settlement was recorded by linear variable displacement transducers. The presence of compressible subgrades below the constructed ballast layers was considered by lining the bottom of the box with one of three rubber mats representing artificial subgrades with equivalent California bearing ratio (CBR) readings of 25, 13, and 5. For each subgrade condition, four ballast box tests were performed with one being conducted on an unreinforced ballast layer, while the remaining three were done on geogrid-reinforced ballast assemblies. The geogrid embedded in the ballast layers was a large aperture biaxial polypropylene geogrid with thick nodes and ribs designed to stabilize coarse unbound aggregates like railroad ballast. The geogrid had square apertures with a center-to-center size of 57 mm and an ultimate tensile strength of 30 kN/m (Desbrousses et al. 2021; Desbrousses & Meguid 2023a; Titan Environmental Containment 2023). The effect of temperature on the geogrid's tensile strength was investigated by Desbrousses et al. (2021, 2023a) who performed in-isolation tensile tests on specimens of the geogrid in a temperature-controlled environment at temperatures ranging from  $-30$  to  $40$  °C. The geogrid's tensile

strength at 2% strain and ultimate tensile strength at temperatures ranging from  $-30$  to  $40$  °C are summarized in Table 1.

For each subgrade, an experiment was performed for geogrid placement depths of 250 mm, 200 mm, and 150 mm below the base of the tie. A diagram of the experimental setup used by Desbrousses et al. (2023) is provided in Fig. 1. The key findings of Desbrousses et al.'s laboratory tests indicated that the subgrade strength yields a considerable influence on the ability of geogrids to reinforce railroad ballast and abate tie settlement. Results demonstrated that geogrid inclusions resulted in similar attenuation of the tie settlement in ballast assemblies supported by a competent subgrade. However, the ability of geogrids to reduce tie settlement showed an increasing sensitivity to the geosynthetic's placement depth as the subgrade became weaker, with geogrids located closer to the tie yielding the highest reductions in tie settlement.

### 3 Discrete Element Modeling of Geogrid-Reinforced Railroad Ballast

The experimental work conducted by Desbrousses et al. (2023) provided insights into the macroscale behavior of tie-ballast assemblies subjected to cyclic loading. This included examining the tie's permanent and resilient settlement, along with the evolution of the ballast layer's stiffness and damping ratio during cyclic loading. However, it was practically impossible to shed light on the particulate-level processes driving these macroscale phenomena. To address this, the current study employs the discrete element (DEM) using Itasca's three-dimensional *Particle Flow Code (PFC 3D)* (Itasca 2022) to investigate the micromechanical aspects of geogrid-ballast interactions that influence the macroscale behavior of geogrid-reinforced ballast. Unlike the continuum assumption used in finite element modeling, DEM allows for a highly discontinuous material such as railroad ballast to be modeled as an assembly of irregularly shaped particles. Particle motion is then calculated using Newton's second law by a time integration approach akin to the central difference method. The interactions between particles are governed by contact models which are particle-interaction laws that rely on sets of contact model parameters to determine the forces arising at particle contacts.

**Table 1** Mechanical properties of the large aperture biaxial polypropylene geogrid

	Temperature (°C)							
	-30	-20	-10	0	10	20	30	40
Tensile strength at 2% strain (kN/m)	18.00	18.11	16.28	16.12	14.61	11.01	10.62	9.54
Ultimate tensile strength (kN/m)	44.85	44.69	43.76	41.03	37.58	33.55	30.77	28.60

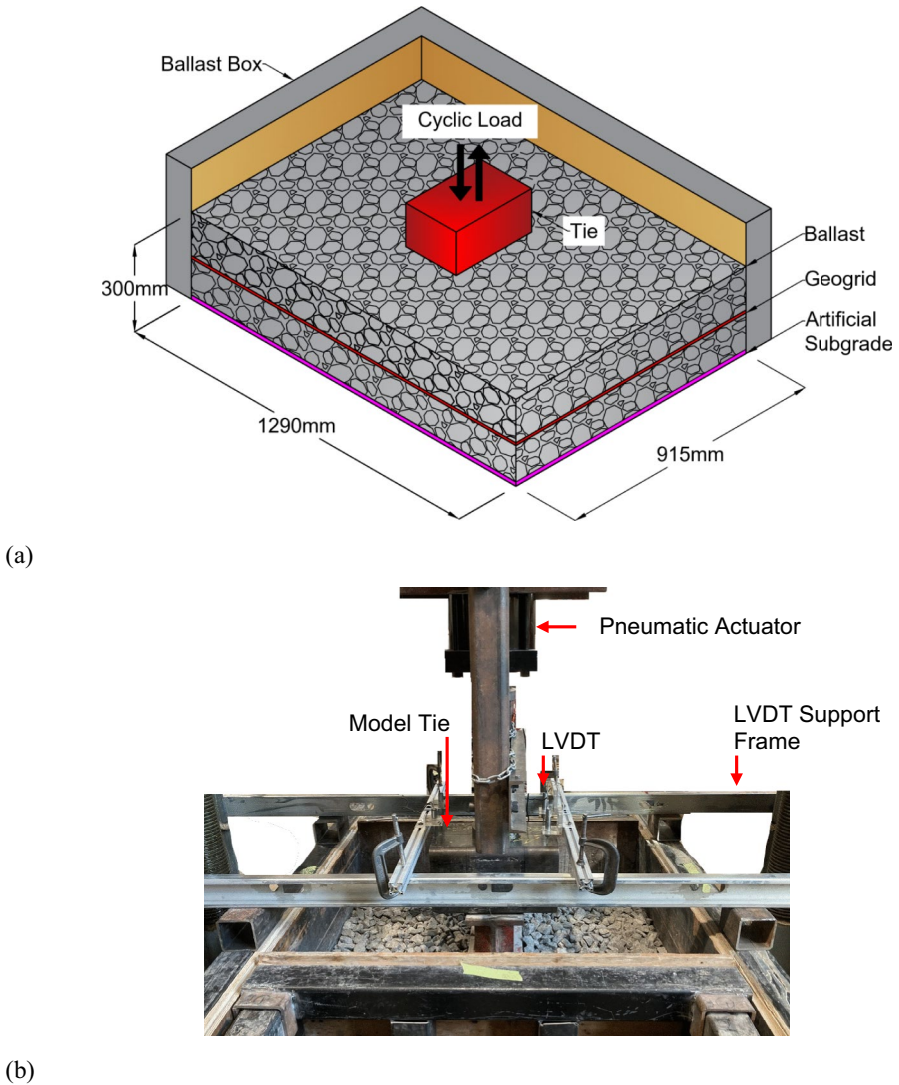


**Fig. 1** **a** Schematic diagram of the ballast box test and **b** laboratory setup used by Desbrousses et al. (2023) (adapted from Desbrousses et al. (2023) with permission)

### 3.1 Railroad Ballast

In discrete element simulations, particle shape yields a significant influence on the simulated material’s bulk behavior. For railroad ballast, researchers commonly use spheres (Gao & Meguid 2018; Guo et al. 2020), polyhedrons (Bian et al. 2020; W. Chen et al. 2023; Qian et al. 2018; Tutumluer et al. 2012), or clumps (assemblies of overlapping spheres) (Chen et al. 2022a, b; H. Li & McDowell 2018; Suhr & Six 2017, 2020, 2022), to represent ballast particles. While spheres are simple and

computationally efficient, they fall short in realistically representing ballast particles due to their round shape and limited contact interlocking. Polyhedrons and clumps, in contrast, can more accurately depict the irregular shapes of ballast particles. Polyhedrons use complex triangular meshes for surface definition, while clumps rely on overlapping spheres of various sizes and positions to approximate a particle's shape. However, as noted by Tolomeo and McDowell (2022), a limitation of polyhedrons in some discrete element codes, like *PFC 3D*, is their requirement to be convex which omits the concavity seen in actual ballast particles. This convexity implies that a polyhedron may only share a single contact with a neighboring polyhedron unlike clumps which can share multiple contact points with neighboring clumps. This gives clumps an enhanced ability to resist rotation and contributes to the formation of a more stable soil structure whereas polyhedrons tend to underestimate the shear strength of railroad ballast (Tolomeo & McDowell 2022).

In this study, the irregular shapes of ballast particles are replicated using the clump logic in *PFC 3D*. This involves scanning a real ballast particle, converting this scan into a 3D triangulated mesh, and then using *PFC 3D*'s *Bubble Pack Algorithm* to create a clump by filling the volume enclosed by the triangular mesh with overlapping spheres of varying size as shown in Fig. 2. The clumps created in this study match the volume of a sphere with a diameter ( $D$ ) of 27.5 mm which corresponds to the mean diameter of the ballast aggregate used in Desbrousses et al.'s experiments (Desbrousses et al. 2023).

The linear contact model is used to represent the interactions between contacting clumps simulating ballast particles as well as between clumps and rigid boundaries such as the ballast box's walls and the tie (C. Chen et al. 2012; Lim & McDowell 2005; Ngo et al. 2014; Zhang et al. 2023). The linear contact model is commonly used in DEM simulations to describe interactions between ballast particles owing to the contact model's simplicity and computational efficiency (Alabbasi & Hussein 2021; C. Chen et al. 2015; Guo et al. 2020; D. Shi et al. 2023). Figure 2c depicts the linear contact model's rheological components which provide the behavior of an infinitesimal linear-elastic and frictional interface that carries a force. When two particles contact, the overlap that develops between the two pieces gives rise to a contact force ( $F_c$ ) which may be resolved into a linear component ( $F^l$ ) and a dashpot component ( $F^d$ ) as follows:

$$F_c = F^l + F^d \quad (1)$$

The linear contact force ( $F^l$ ) consists of a normal ( $F_n^l$ ) and tangential ( $F_s^l$ ) component and may be expressed as follows:

$$F^l = -F_n^l n_c + F_s^l \quad (2)$$

where  $n_c$  is the unit vector that defines the contact plane.

The linear normal force ( $F_n^l$ ) and tangential force ( $F_s^l$ ) are produced by linear springs with constant normal ( $k_n$ ) and shear ( $k_s$ ) stiffnesses, respectively. Slip between contacting particles is permitted by imposing a Coulomb limit on the shear force. During a given timestep  $\Delta t$ ,  $F_n^l$  is updated based on the surface gap ( $g_s$ ) between contacting particles while  $F_s^l$  is updated incrementally based on the shear



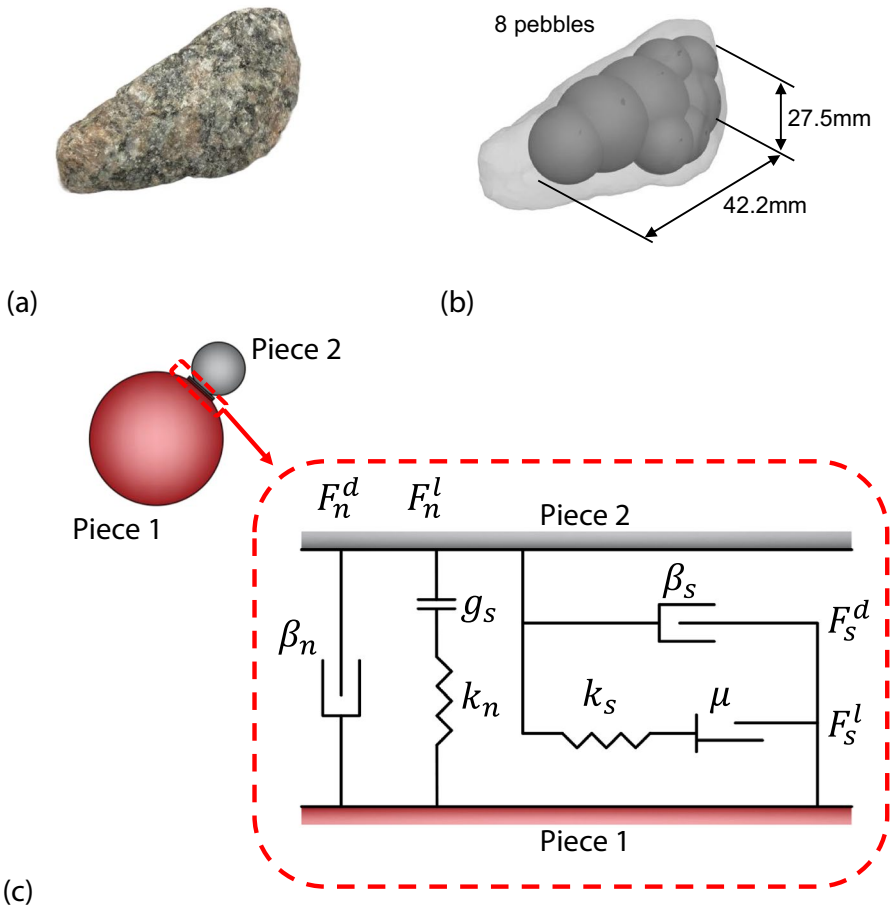


**Fig. 2** Modeling ballast particles using the clump logic: **a** ballast particle, **b** PFC 3D clump, and **c** linear contact model and its rheological components

component ( $\Delta\delta_s$ ) of the relative displacement increment between the contacting particles.

The normal force is calculated as follows:

$$F_n^l = k_n g_s, g_s < 0 \tag{3}$$

The shear force is then updated by first calculating a trial shear force:

$$F_s^* = (F_s)_0 - k_s \Delta\delta_s \tag{4}$$

where  $(F_s)_0$  is the shear force at the beginning of the timestep and  $(\Delta\delta_s)$  is the relative shear displacement increment. The trial shear force is compared with the contact's shear strength:

$$F_s^\mu = -\mu F_n \quad (5)$$

where  $\mu$  is the friction coefficient. The shear force is then updated as follows:

$$F_s^l = \begin{cases} F_s^*, & \text{if } \|F_s^*\| \leq F_s^\mu \\ F_s^\mu \left( \frac{F_s^*}{\|F_s^*\|} \right) & \end{cases} \quad (6)$$

The normal and shear spring stiffnesses are related to one another through the effective modulus ( $E^*$ ) and the normal-to-shear stiffness ratio ( $\kappa^*$ ) using the following relationships (Itasca 2022):

$$k_n = \frac{AE^*}{L} \quad (7)$$

$$\kappa^* = \frac{k_n}{k_s} \quad (8)$$

where  $A$  is the contact area between two contacting pieces and  $L$  is the distance between the centroid of contacting pieces:

$$A = \pi r^2 \quad (9)$$

$$r = \begin{cases} \min(R^{(\text{piece1})}, R^{(\text{piece2})}), & \text{ball - ball} \\ R^{\text{piece1}}, & \text{ball - wall} \end{cases} \quad (10)$$

$$L = \begin{cases} R^{(\text{piece1})} + R^{(\text{piece2})}, & \text{ball - ball} \\ R^{(\text{piece1})}, & \text{ball - wall} \end{cases} \quad (11)$$

And  $R$  denotes the radius of the contacting balls.

To simulate the behavior of railroad ballast, the linear contact model's effective modulus ( $E^*$ ) and normal-to-shear stiffness ratio ( $\kappa^*$ ) are calibrated by simulating three large-scale triaxial tests conducted by Suiker et al. (2005) on AREMA No. 4 ballast. The triaxial tests were performed on cylindrical ballast samples with a diameter of 254 mm and a height of 645 mm (see Fig. 3a) at confining pressures of 10.3 kPa, 41.3 kPa, and 69.8 kPa. Suiker et al. reported their results by computing the stress ratio  $-(q/p)$  and the deviatoric strain ( $\kappa$ ), where  $q$  is the deviatoric stress invariance and  $p$  is the hydrostatic stress invariant. The aforementioned variables are computed as follows:

$$q = |\sigma_1 - \sigma_3| = \sigma_d \quad (12)$$

$$p = \frac{1}{3}(\sigma_1 + 2\sigma_3) \quad (13)$$

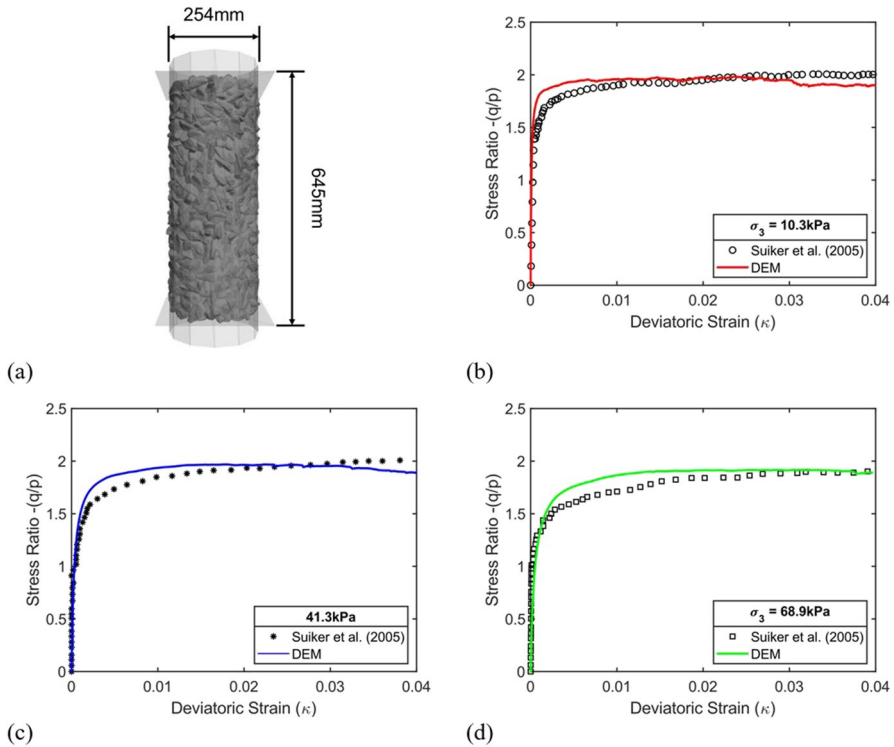


**Fig. 3** a Simulating the triaxial tests performed by Suiker et al. (2005) and comparing the experimental data with the discrete element simulations at confining pressures of **b** 10.3 kPa, **c** 41.3 kPa, and **d** 68.9 kPa

$$\kappa = \frac{2}{3} |e_1 - e_3| \tag{14}$$

where  $\sigma_1$  is the major principal stress,  $\sigma_3$  is the minor principal stress,  $\sigma_d$  is the deviatoric stress,  $e_1$  is the major principal strain, and  $e_3$  is the minor principal strain.

The results obtained experimentally are compared with the results from the DEM triaxial tests in Fig. 3b to c. The discrete element simulations exhibit a reasonable agreement with the experimental data, giving an effective modulus  $E^*$  of 325 MPa, a normal-to-shear stiffness ratio ( $\kappa^*$ ) of 1, and a friction coefficient ( $\mu$ ) of 0.55. The contact model parameters are summarized in Table 2.

### 3.2 Geogrid

To capture the micromechanical features of the geogrid-ballast interaction mechanisms numerically, the large aperture biaxial polypropylene geogrid used by Desbrousses et al. (2023) in their experimental work is modeled. The geogrid’s discrete element model is created following the grid generation procedure developed by Stahl et al. (2014) and Itasca (2019) in which geogrids are modeled as strings of overlapping

**Table 2** Contact model parameters used for the ballast particles and the box's walls

Parameter	Value
Clumps (ballast)	
Particle density, $\rho$ (kg/m <sup>3</sup> )	2741
Effective modulus, $E^*$ (MPa)	325
Normal-to-shear stiffness ratio, $\kappa^*$	1
Friction coefficient, $\mu$	0.55
Facets (side walls)	
Effective modulus, $E^*$ (MPa)	325
Normal-to-shear stiffness ratio, $\kappa^*$	1
Friction coefficient, $\mu$	0.55
Facets (bottom wall)	
CBR = 25	
Normal and shear stiffnesses, $k_n, k_s$ (N/m)	$1 \times 10^6$
Friction coefficient, $\mu$	0.55
CBR = 5	
Normal and shear stiffnesses, $k_n, k_s$ (N/m)	$2 \times 10^5$
Friction coefficient, $\mu$	0.55

spheres joined by linear parallel bonds as shown in Fig. 4. The geogrid's constitutive behavior is represented by the linear parallel bond contact model. The linear parallel bond contact model provides the behavior of two interfaces and simulates the presence of cementing material between two contacting particles. The first interface is analogous to the linear contact model insofar as it carries a force, does not resist relative particle rotation, and permits slippage by applying a Coulomb limit on the shear force. The

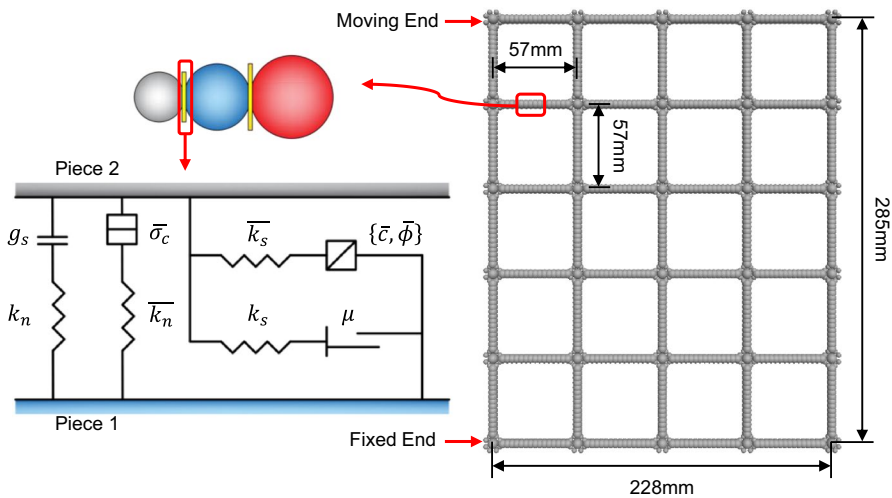


**Fig. 4** Discrete element model of the biaxial geogrid showing the boundary conditions used in the multi-rib tensile test and the rheological components of the linear parallel bond contact model

second interface, called the parallel bond, acts in tandem with the first one. It establishes an elastic interaction between contacting particles that transmits both a force and a moment through a set of elastic springs distributed over the contact plane. The linear parallel bond model updates the contact force ( $F_c$ ) and moment ( $M_c$ ) as follows:

$$F_c = F^l + F^d + \bar{F} \tag{15}$$

$$M_c = \bar{M} \tag{16}$$

where  $F^l$  is the linear force,  $F^d$  is the dashpot force, and  $\bar{F}$  is the parallel-bond force. The parallel-bond force is composed of a normal ( $\bar{F}_n$ ) and shear component ( $\bar{F}_s$ ), while the parallel-bond moment is resolved into a twisting ( $\bar{M}_t$ ) and bending moment ( $\bar{M}_b$ ), giving the following:

$$\bar{F} = -\bar{F}_n n_c + \bar{F}_s \tag{17}$$

$$\bar{M} = \bar{M}_t n_c + \bar{M}_b \tag{18}$$

The parallel-bond force and moment are then updated as follows:

$$\bar{F}_n = \bar{F}_n + \bar{k}_n \bar{A} \Delta \delta_n \tag{19}$$

$$\bar{F}_s = \bar{F}_s - \bar{k}_s \bar{A} \Delta \delta_s \tag{20}$$

where  $\Delta \delta_n$  is the relative normal displacement increment,  $\bar{A}$  is the parallel bond's cross-sectional area,  $\bar{k}_n$  is the parallel bond's normal spring stiffness,  $\Delta \delta_s$  is the relative shear displacement increment, and  $\bar{k}_s$  is the parallel bond's shear spring stiffness.

$$\bar{M}_t = \bar{M}_t - \bar{k}_s \bar{J} \Delta \theta_t \tag{21}$$

$$\bar{M}_b = \bar{M}_b - \bar{k}_n \bar{I} \Delta \theta_b \tag{22}$$

where  $\bar{I}$  and  $\bar{J}$  are the parallel bond cross section's moment of inertia and polar moment of inertia respectively and  $\Delta \theta_t$  and  $\Delta \theta_b$  are the relative twist and bend-rotation increments, respectively. The maximum normal ( $\sigma_{max}$ ) and shear ( $\tau_{max}$ ) stresses at the parallel-bond periphery may be obtained as follows:

$$\sigma_{max} = \frac{\bar{F}_n}{\bar{A}} + \frac{\|\bar{M}_b\| \bar{R}}{\bar{I}} \tag{23}$$

$$\tau_{max} = \frac{\|\bar{F}_s\|}{\bar{A}} + \frac{|\bar{M}_t| \bar{R}}{\bar{J}} \tag{24}$$

where  $\bar{R}$  is the parallel bond radius.

The parallel bond contact parameters are defined using the deformability method, whereby the bond's normal and tangential spring stiffnesses ( $\overline{k}_n$  and  $\overline{k}_s$ ) are characterized by the bond effective modulus ( $\overline{E}^*$ ) and the bond normal-to-shear stiffness ratio ( $\overline{\kappa}^*$ ) where:

$$\overline{k}_n = \frac{\overline{E}^*}{L} \quad (25)$$

$$\overline{k}_s = \frac{\overline{k}_n}{\overline{\kappa}^*} \quad (26)$$

$$L = \left\{ \begin{array}{ll} R^{(\text{ball}1)} + R^{(\text{ball}2)}, & \text{ball - ball} \\ R^{(\text{ball}1)}, & \text{ball - wall} \end{array} \right\} \quad (27)$$

where  $L$  is the distance between the centroid of contacting pieces.

The linear parallel bond contact model parameters are calibrated by simulating a single-rib tensile test, a multi-rib tensile test, and an aperture stability modulus test and comparing the results with the tensile test data published by Desbrousses et al. (2021, 2023a) and the aperture stability modulus provided by the geogrid's manufacturer (Titan Environmental Containment 2023). Given that the parallel bond provides the behavior of a linear elastic cementing material between contacting particles, the viscoelastic behavior typically displayed by polymeric geogrids may not be captured in the simulated tensile tests. As such, the contact model parameters are calibrated to match the geogrid's tensile strength at 2% strain due to the almost linear relationship between force and elongation exhibited by the biaxial geogrid during tensile testing (Gao & Meguid 2018; Han et al. 2012; McDowell et al. 2006; Ngo et al. 2014). The single-rib and multi-rib tensile tests are simulated to comply with the requirements outlined in ASTM D6637 methods A and B, respectively.

The simulated geogrid consists of thick longitudinal and transverse ribs composed of 15 overlapping spheres with a radius of 3 mm. The nodes are represented by larger spheres with a radius of 3.5 mm each surrounded by eight smaller node balls with a radius of 1.75 mm to give the junction the required torsional stiffness. The geogrid specimen used in the single-rib tensile test simulation is 285 mm long and comprises six junctions thereby closely matching the dimensions of the geogrid specimens used in the tensile tests performed by Desbrousses et al. (2021, 2023a). Similarly, the multi-rib geogrid specimens used in the multi-rib tensile test simulation are 285 mm long and 228 mm wide, having six junctions in the direction of testing as shown in Fig. 4. Both the single-rib and multi-rib tensile tests are performed by fully restraining the motion of the bottom rib of the tested sample and applying a constant velocity corresponding to a strain rate of 10% strain/min in the testing direction to the topmost rib or rib junction. The results from the numerical tensile tests are compared with the available experimental data for geogrids tested at room temperature (20 °C) in Fig. 5a and b. In order to investigate the effect of geogrid stiffness on the grid's ability to stabilize railroad ballast, additional tensile tests are simulated and compared with the geogrid's 2% strain tensile strength determined at

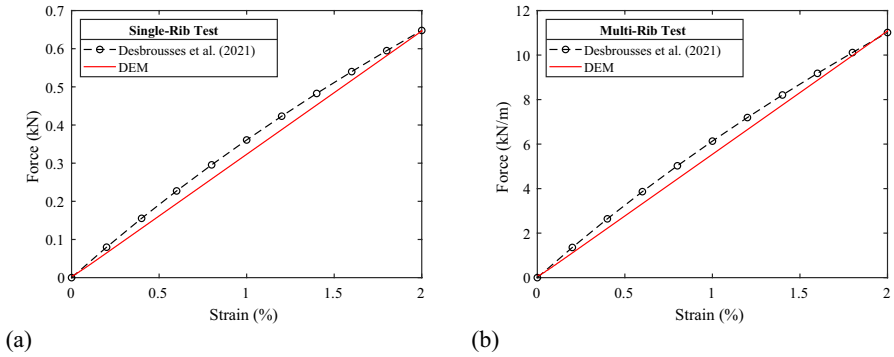


**Fig. 5** Comparing experimental data obtained by Desbrousses et al. (2021) with the discrete element simulations of the (a) single-rib and (b) multi-rib tensile tests

−30, −10, 10, 20, and 40 °C by Desbrousses et al. (2021, 2023a). The corresponding contact model parameters are summarized in Table 3. It is noteworthy that the linear parallel bond contact model’s effective modulus  $E^*$  is set to a very low value to preclude the development of large contact forces between the geogrid’s overlapping spheres.

**Table 3** Contact model parameters used for the biaxial geogrid

Parameter	Value
<b>Geogrid</b>	
Particle density, $\rho$ (kg/m <sup>3</sup> )	950
Effective modulus, $E^*$ (MPa)	$1 \times 10^{-8}$
Normal-to-shear stiffness ratio, $k^*$	1
Tensile strength, $\bar{\sigma}_c$ (MPa)	$1 \times 10^{14}$
Cohesion, $\bar{c}$ (MPa)	$1 \times 10^{14}$
$T = -30$ °C	
Bond effective modulus, $\bar{E}^*$ (MPa)	750
Bond normal-to-shear stiffness ratio, $\bar{k}^*$	1
$T = -10$ °C	
Bond effective modulus, $\bar{E}^*$ (MPa)	680
Bond normal-to-shear stiffness ratio, $\bar{k}^*$	1
$T = 10$ °C	
Bond effective modulus, $\bar{E}^*$ (MPa)	610
Bond normal-to-shear stiffness ratio, $\bar{k}^*$	1
$T = 20$ °C	
Bond effective modulus, $\bar{E}^*$ (MPa)	465
Bond normal-to-shear stiffness ratio, $\bar{k}^*$	1
$T = 40$ °C	
Bond effective modulus, $\bar{E}^*$ (MPa)	400
Bond normal-to-shear stiffness ratio, $\bar{k}^*$	1

The modeled geogrid's torsional stiffness is assessed by simulating an aperture stability modulus test following the procedure outlined in ASTM D7864 in which a square geogrid sample is generated and clamped along its four outer edges as shown in Fig. 6a. The central junction is then subjected to a twisting moment ( $M_t$ ) of 2 N m by applying a force ( $F$ ) to each of the four ribs emanating from the junction at points located at a distance ( $r$ ) of  $12.7 \text{ mm} \pm 1 \text{ mm}$  away from it. The geogrid's torsional stiffness ( $k_t$ ) is then calculated by dividing the twisting moment ( $M_t$ ) by the resulting rotation ( $\theta_t$ ) as follows:

$$k_t = \frac{M_t}{\theta_t} \quad (28)$$

For the chosen contact model parameters, the application of a twisting moment of 2 N m caused a rotation of  $2.67^\circ$  (see Fig. 6b), giving a torsional stiffness of 0.748 N m/deg which closely matches the 0.75 N m/deg reported by the geogrid's manufacturer (Titan Environmental Containment 2023). The contact model parameters used for the geogrid are presented in Table 3. It is important to point out that the interactions between the geogrid, ballast particles, and walls are described by the linear contact model using the same contact model parameters as those used for ballast particles.

### 3.3 Ballast Box and Geogrid-Ballast Assemblies

A ballast box with plan dimensions identical to those used by Desbrousses et al. (2023) in their experiments is created in *PFC 3D* using facets (i.e., walls). The linear contact model is used to characterize the interactions between the ballast particles and the box's walls using contact parameters identical to those used for the ballast particles (C. Chen et al. 2012, 2015; H. Li & McDowell 2020, 2018; Lim & McDowell 2005). A 300-mm-thick ballast layer is then generated in six 50-mm-thick lifts using the improved multi-layer compaction method (IMCM) developed by Lai et al. (2014) and used in multiple discrete element studies to generate geogrid-reinforced soil samples (J. Chen, Bao, et al. 2022a, b; Gao & Meguid 2018; Lai et al. 2014). The sample generation process takes place in a gravity-free environment with the friction coefficient set to zero for the clumps and the facets. The first lift is created by generating a cloud of non-overlapping clumps in the box and compressing it using a rigid platen until the desired porosity is reached, at which point the model is cycled to equilibrium. The second lift is then generated in a similar fashion, compressed above the first lift using a second rigid platen, and cycled to equilibrium at which point the wall separating the two lifts is deleted and the model is cycled to equilibrium again. The process is repeated until the desired height of the ballast layer is reached. When a geogrid is to be incorporated in the ballast layer and its placement depth is attained during the sample generation process, a geogrid with plan dimensions of  $1000 \times 700 \text{ mm}$  is created within a sleeve consisting of two rigid walls to preclude contacts between the grid and the surrounding clumps during the generation process. The grid balls are then fixed such that they may not translate nor rotate. A subsequent



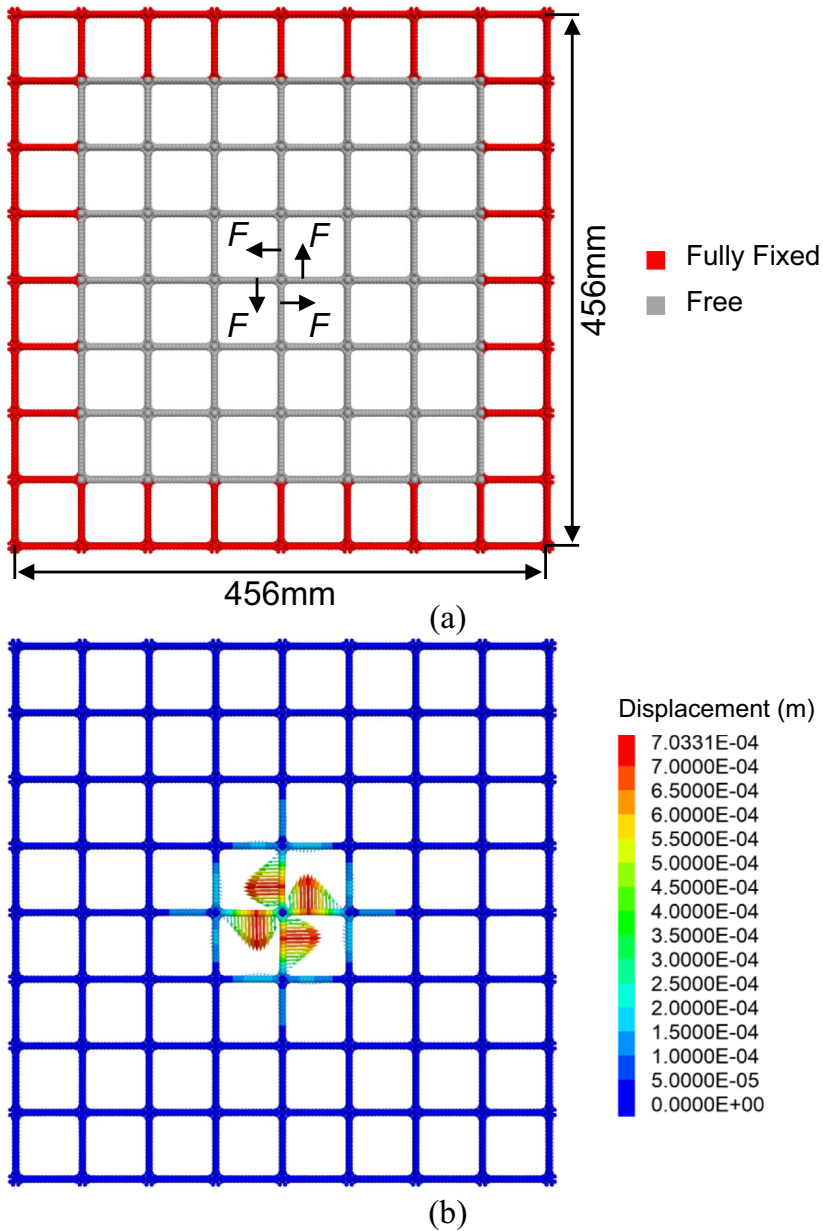


**Fig. 6** **a** Boundary conditions used in the aperture stability modulus test and **b** displacement of the geogrid ribs following the application of the twisting moment

ballast layer is then created above the geogrid, compressed to the desired porosity, and cycled to equilibrium. The geogrid’s protective sleeve is then removed, allowing it to come into contact with the surrounding ballast particles. Once the

ballast sample is fully generated, gravity is turned on, the coefficient of friction for the clumps, facets, and geogrid balls is set to its final value, the geogrid balls are freed such that the geogrid may deform freely within the ballast sample, and the model is cycled to equilibrium. A tie with plan dimensions of  $203 \times 301$  mm is then placed at the top of the compacted granular assembly. The sample generation process is illustrated in Fig. 7.

To simulate the presence of subgrades with equivalent California bearing ratios (CBRs) of 25 and 5 beneath the ballast layer, the contact stiffness ( $k_n$ ) of the ballast box's bottom wall is calibrated. This involves subjecting unreinforced ballast layers to cyclic loading with a mean compressive load of 14 kN, a loading amplitude of 10.5 kN, and a frequency of 0.8 Hz for 20 cycles. The settlement response of the tie is then compared with the experimental results published by Desbrousses et al. as shown in Fig. 8. This comparison helps determine the suitable spring stiffness values for the box bottom wall, which is summarized in Table 2.

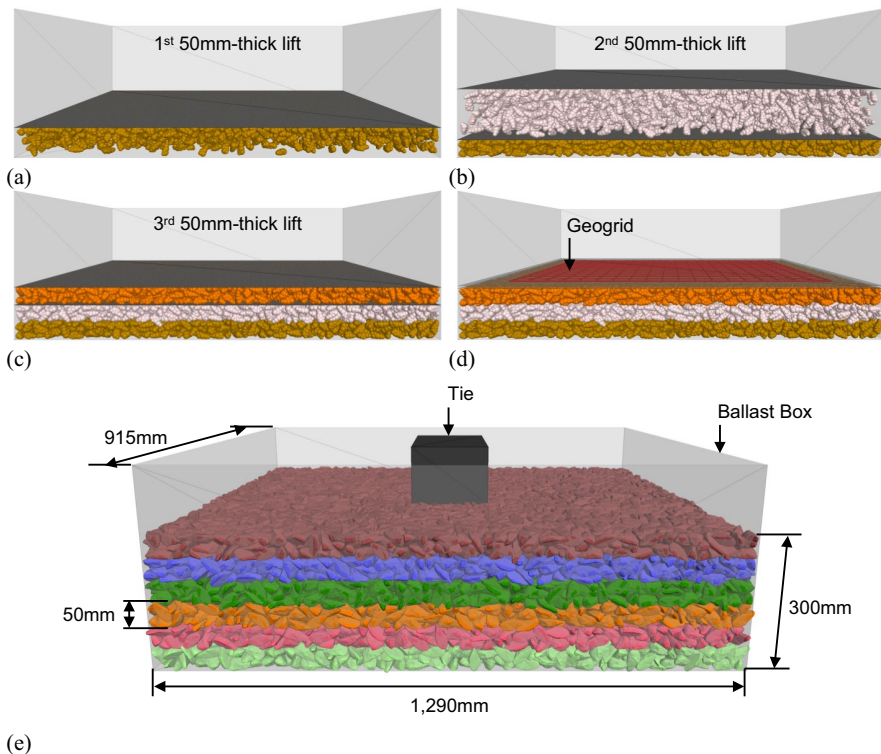


**Fig. 7** Sample generation procedure using the improve multi-layer compaction method (IMCM) showing the **a** generation of the first 50-mm-thick lift, **b** creation of the second lift, **c** compaction of the third lift, **d** incorporation of a geogrid 150 mm above the base of the box, and **e** compacted 300-mm-thick ballast layer

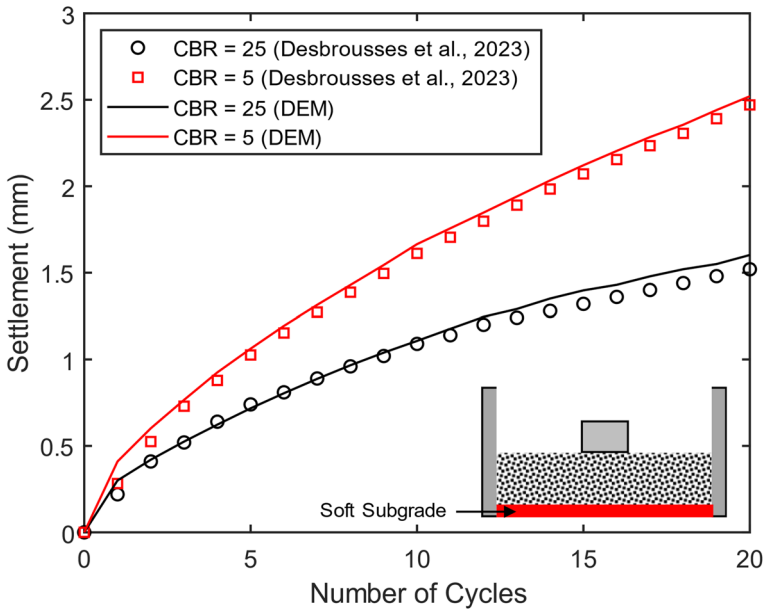


**Fig. 8** Calibrating the box's bottom wall's spring stiffness to simulate the presence of subgrades with CBRs of 25 and 5 below the ballast layer

### 3.4 Simulation Summary

In this study, each ballast box simulation involves the application of cyclic loading to the tie for 20 load cycles at a frequency of 10 Hz with a mean load of 14 kN and a load amplitude of 10.5 kN. Two subgrade conditions are considered, with CBRs of 25 and 5. For each subgrade, six ballast box tests are carried out: one with an unreinforced ballast layer and five with geogrid-reinforced ballast assemblies, where the geogrid is placed at depths ranging from 50 to 250 mm below the tie, in 50 mm intervals. This setup is chosen to assess how different geogrid placement depths affect the mechanical properties of geogrid-reinforced ballast. Upon investigating the effect of the geogrid placement depth, the influence of the geogrid aperture size ( $A$ ) and geogrid stiffness is studied. The geogrid aperture size is varied from  $30 \times 30$  to  $80 \times 80$  mm, giving rise to aperture-size-to-ballast-diameter ( $A/D$ ) ratios from 1.09 to 2.91, while the geogrid stiffness is set to values ranging from 9.54 to 18.00 kN/m. An overview of the simulations presented in this paper is provided in Table 4.

It is imperative to clarify that the primary objective of these simulations is not to replicate the exact outcomes observed in Desbrousses et al.'s experimental work. Instead, the discrete element simulations presented herein are exploratory in nature and are strategically designed to delve into the intricate micromechanical features of ballast-geogrid interactions. All micromechanical contact parameters employed in these simulations have been rigorously calibrated using existing experimental data, ensuring a robust and realistic representation of the physical behavior of the materials involved. The focus of this study is on qualitatively examining the underlying

**Table 4** Simulation summary

Subgrade strength (CBR)	Geogrid depth (mm)	A/D ratio	Geogrid stiffness (kN/m)
25	50, 100, 150, 200, 250	2.07	11.01
5	50, 100, 150, 200, 250	2.07	11.01
5	150	1.09, 1.45, 1.82, 2.07, 2.55, 2.91	11.01
5	150	2.07	18.00, 16.28, 14.61, 11.01, 9.54

mechanisms influencing the behavior of geogrid-reinforced ballast under cyclic loading, particularly in terms of particle displacement, rotation, velocity, and the development of interparticle contacts. Deliberate variations in the loading frequency and the number of load cycles allow for a broader exploration of simulation scenarios, thereby enhancing the study's scope while keeping the simulation time within reasonable limits.

## 4 Results and Analysis

### 4.1 Macroscopic Behavior

The macroscale response of ballast layers supported by subgrades with a CBR of 25 and 5 is investigated by analyzing the evolution of the tie's settlement shown in Fig. 9a and b, respectively. In ballast box tests performed over a competent subgrade (CBR of 25), the largest tie settlement takes place in the unreinforced ballast layer, culminating at a value of 7.83 mm after 20 load cycles. The tie's permanent displacement decreases following the introduction of a geogrid in the ballast layer, although this reduction is sensitive to the geosynthetic's placement depth. At the end of the 20 load cycles, the tie resting on ballast assemblies reinforced with geogrids placed at depths of 200 mm and 250 mm settles by 6.45 mm and 6.31 mm

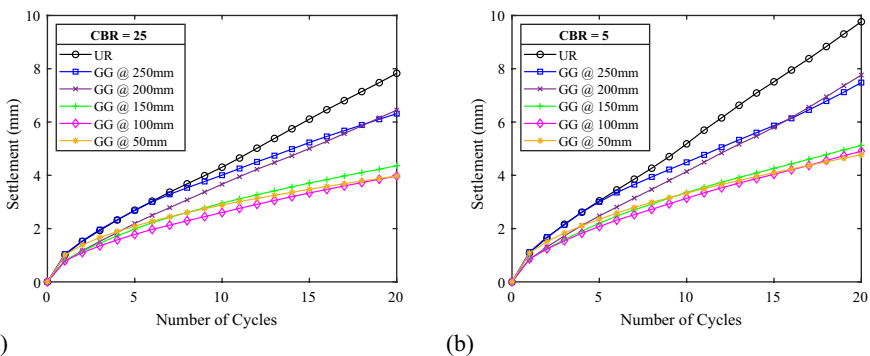


**Fig. 9** Accumulation of tie settlement in unreinforced and geogrid-reinforced ballast layers supported by a subgrade with a CBR of (a) 25 and (b) 5

mm, respectively, which represents respective settlement reductions of 17.67% and 19.34% compared to the unreinforced case. Incorporating a geogrid at a shallower location in the ballast layer, i.e., 50 mm, 100 mm, and 150 mm beneath the tie, leads to markedly smaller tie settlements of 3.97 mm, 3.97 mm, and 4.36 mm, representing settlement reductions of 49.23%, 49.26%, and 44.27% respectively compared to the unreinforced ballast layer.

Greater tie settlements invariably develop in ballast layers supported by a weaker subgrade (CBR of 5) as illustrated by Fig. 9b. Similar to the trends observed in the ballast beds overlying a subgrade with a CBR of 25, the maximum tie settlement occurs in the unreinforced ballast assembly, reaching a total value of 9.76 mm. The reduction in tie settlement generated by the placement of a geogrid in the ballast layer exhibits features akin to those encountered in ballast box tests performed on a more competent subgrade. Geogrids placed deep into the ballast layer, i.e., 200 mm and 250 mm below the tie, are less effective at minimizing the tie’s settlement compared with geogrids positioned within the layer’s upper 150 mm. The lowest reductions in tie settlement of 23.37% and 20.38% are obtained in ballast assemblies reinforced with geogrids located 250 mm and 200 mm beneath the tie, respectively. However, incorporating geogrids at depths of 50 mm, 100 mm, and 150 mm results in respective tie settlement reductions of 51.15%, 49.81%, and 47.55%. It is also noteworthy that, on average, greater reductions in tie subsidence are achieved by geogrids when the underlying subgrade is weak.

The settlement curves shown in Fig. 9 indicate that not all ballast layers exhibit the same rate of settlement growth as the number of load cycles increases. Indeed, the unreinforced ballast layers along with the ones reinforced with geogrids placed 200 mm and 250 mm below the tie possess a steeper rate of settlement accumulation than that of geogrid-reinforced ballast beds where geogrids are located in the upper 150 mm. To examine this pattern, the incremental non-recoverable vertical tie displacement recorded in ballast assemblies supported by subgrades with a CBR of 25 and 5 is plotted in Fig. 10a and b, respectively.

Figure 10a and b indicate that all ballast samples initially undergo significant residual settlement following the application of the first load cycle. This is then

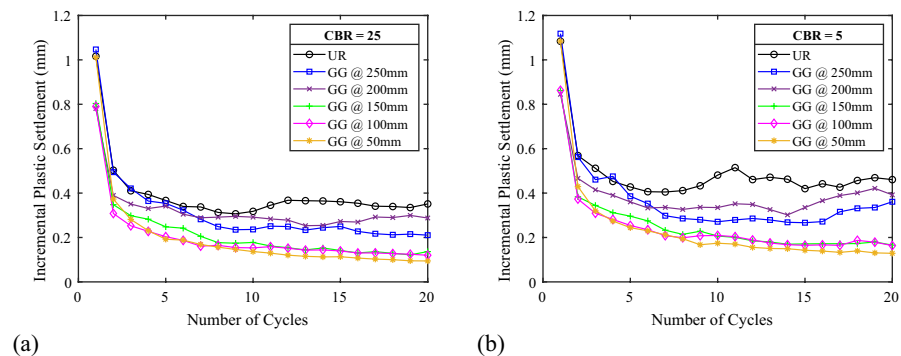


**Fig. 10** Variations in the incremental tie settlement with cyclic loading in unreinforced and geogrid-reinforced ballast layers supported by a subgrade with a CBR of (a) 25 and (b) 5

followed by a progressive decline in the rate at which residual settlement accumulates under further cyclic loading. Interestingly, ballast beds reinforced with geogrids positioned at depths of 50 mm, 100 mm, and 150 mm see their incremental residual tie settlement stabilize as the number of cycles increases. This suggests that these layers gradually reach a stable state in which the large initial tie subsidence was caused by significant rearrangements of the soil fabric as ballast particles moved and slid past each other to form a denser state. However, this phenomenon is not observable in the unreinforced ballast layers nor the ballast beds reinforced with geogrids located 200 mm and 250 mm under the tie. The incremental tie settlement in these three cases fluctuates as cyclic loading continues, particularly in the case of a weak subgrade (CBR of 5). These variations suggest that considerable rearrangement of the soil fabric keeps occurring as cyclic loading continues and hint at the fact that these ballast assemblies are likely to experience a sustained accumulation of residual tie settlement under further repeated loading while simultaneously highlighting the superior settlement-abating ability of geogrids situated within the upper 150 mm of the ballast layers.

The results presented in Figs. 9 and 10 illustrate the macroscopic manifestations of the incorporation of biaxial geogrids in 300-mm-thick ballast layers. The deformation response of geogrid-reinforced ballast is particularly sensitive to the placement depth of geogrid reinforcement, with geogrids positioned closer to the tie yielding greater reductions in tie settlement. Additionally, although greater settlement magnitudes are recorded in ballast assemblies resting on a subgrade with a CBR of 5, similar deformation patterns develop ballast samples supported by the two subgrades considered in this section.

In the following sections, a microscopic analysis is conducted to explore the micromechanical behavior of unreinforced and geogrid-reinforced ballast subjected to cyclic loading. A particular emphasis is placed on investigating the impact of geogrids on the ballast particles' translational and rotational motion, coordination number, contact orientation, and the energy dissipated through frictional sliding during cyclic loading. For the sake of brevity and given the similar patterns observed in ballast layers supported by subgrades with CBRs of 25 and 5, the analysis is confined to the ballast box tests performed over a subgrade with a CBR of 5.

## 4.2 Microscale Response

### 4.2.1 Particle Displacement Vectors

To study the reinforcing mechanisms involved in the behavior of geogrid-reinforced ballast, the motion of the ballast particles contained in the ballast box is examined. The total displacement vectors of ballast particles in the unreinforced and geogrid-reinforced ballast box tests obtained during the 20th load cycle are plotted at the same scale in Fig. 11a to f.

The displacement vectors provide a first glimpse into the micromechanical processes involved in the evolution of the tie settlement observed in Fig. 9. Among all the ballast box experiments, the tie resting on the unreinforced ballast layer

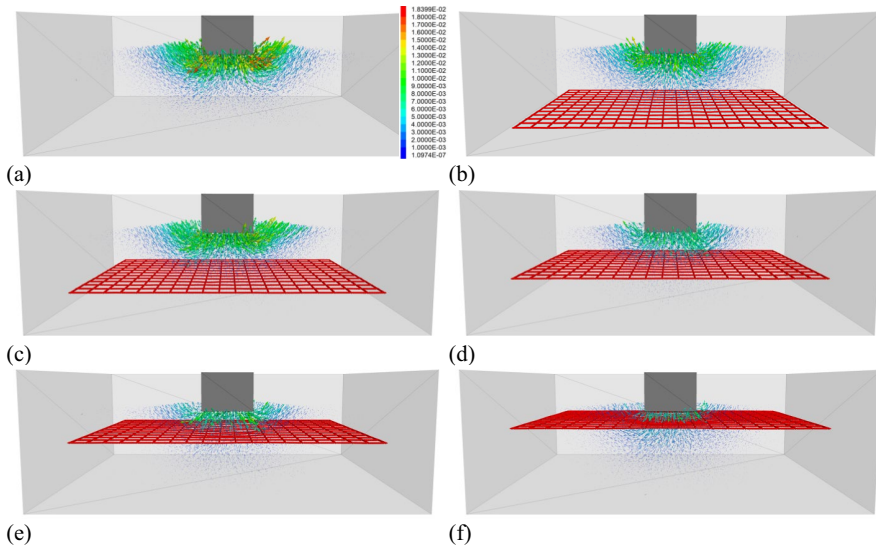


**Fig. 11** Total displacement vectors plotted at the same scale during the 20th load cycle in the **a** unreinforced ballast layer and geogrid-reinforced ballast layers with geogrids located at depths of **b** 250 mm, **c** 200 mm, **d** 150 mm, **e** 100 mm, and **f** 50 mm

experiences the highest cumulative settlement. Fig. 11a illustrates the effect of this subsidence at the particle level, where the displacement vectors of the particles are noticeably larger than those in geogrid-reinforced ballast assemblies. Furthermore, the most significant particle displacements occur in the layer's upper half. Directly beneath the tie, ballast aggregates primarily exhibit vertical movements, while particles on the tie's sides predominantly displace laterally. In contrast, the lower half of the ballast assembly experiences comparatively smaller particle displacements. This indicates the existence of an active zone, marked by substantial particle movement within the top 150 mm of the ballast layer, and a stable zone in the lower half, characterized by minimal particle movement.

Incorporating geogrids at depths of 250 mm and 200 mm, as shown in Fig. 11b and c, results in modest decreases in the magnitude of the particle displacement vectors. Substantial particle movement persists in the ballast bed's upper half, with notable lateral displacements in particles adjacent to the tie. While the geogrids do mitigate particle motion, the reduction is somewhat limited, aligning with the observed accumulation of tie settlement in Fig. 9b.

Figure 11 d to f highlight the impact of the geogrid placement depth on tie settlement. Figure 11d demonstrates that positioning a geogrid 150 mm beneath the tie significantly alters the particle displacement vectors, changing both the magnitude and the direction of particle movement. The most noticeable shifts occur around the tie, with reduced lateral displacements compared to both the unreinforced ballast bed and samples with geogrids at depths of 200 mm and 250 mm. This suggests that the closer the geogrid is to the active zone, the more effectively it curtails particle movement, particularly limiting lateral displacements. Figure 11e and

f, illustrating ballast layers reinforced with geogrids placed at depths of 100 mm and 50 mm, respectively, support this observation. A notable trend emerges, whereby as the geogrid is placed nearer to the tie, there is a progressive decrease in the magnitude of the displacement vectors, especially in lateral movements, reaching a peak efficacy with the geogrid positioned 50 mm below the tie.

From a practical perspective, the observed reductions in lateral particle displacement can be tied to the lateral flow of ballast particles observed in typical ballasted tracks. Railroad ballast is essentially a self-supporting material that is generally exposed to low confining pressures (i.e., 5–40 kPa) (Hussaini et al. 2015; Hussaini & Sweta 2021; Indraratna et al. 2005; Lackenby et al. 2007; Thakur et al. 2013). The absence of lateral resisting forces allows ballast particles to spread laterally when subjected to cyclic loading, leading to an increase in track deformation and ballast degradation (Hussaini et al. 2016; Indraratna et al. 2005; Selig & Waters 1994). Analyzing the lateral displacement of ballast particles in the simulated ballast box tests demonstrates the ability of geogrids to laterally confine unbound granular materials like ballast through the formation of a geogrid-ballast interlock that resists the particles' lateral movement. This reduction in lateral displacement then translates into the tie undergoing a smaller total settlement.

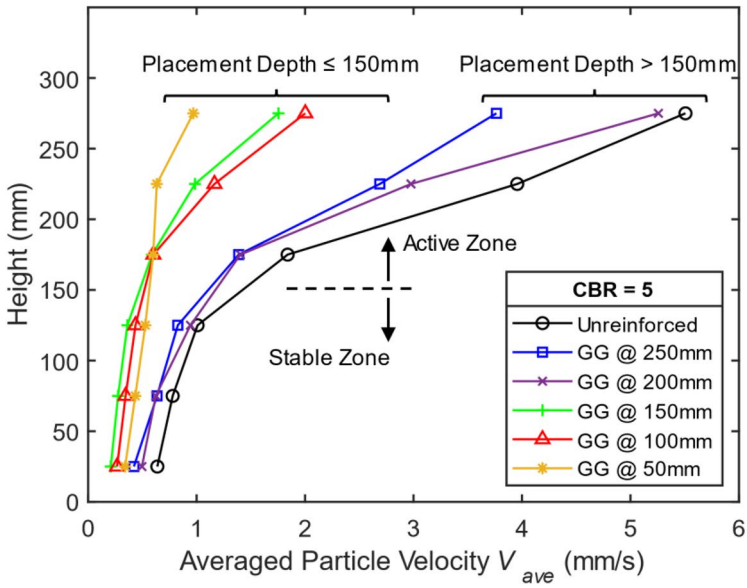
#### 4.2.2 Particle Translational and Rotational Motion

Figure 12 illustrates the average particle velocity across the height of each 300-mm-thick ballast layer. In every scenario, particle velocity increases steadily from the base of the box up to 150 mm, aligning with the stable zone of minimal particle displacement observed in Fig. 11a to f. Above 150 mm, the average particle velocity increases significantly, corresponding to the active zone of intense particle displacement. The unreinforced ballast layer shows the highest particle velocities throughout its height compared to the geogrid-reinforced granular assemblies, peaking at 5.51 mm/s near the top.

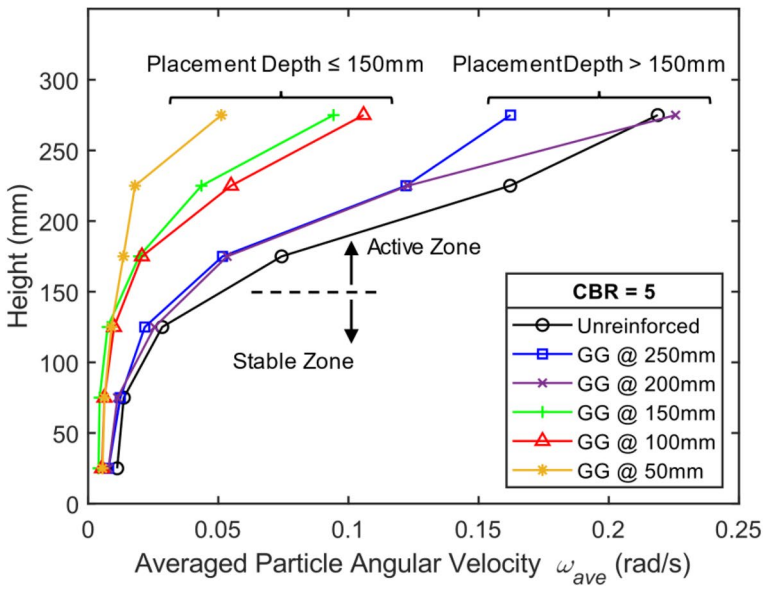
For layers with geogrids at 200 mm and 250 mm depths, the pattern of particle velocity change is similar to that of the unreinforced layer, albeit with lower overall magnitudes. Below 150 mm, velocities in these layers are nearly identical. Above this height, both layers exhibit a substantial increase in average particle velocity, with the layer containing a geogrid at 200 mm showing a slightly higher maximum velocity of 5.26 mm/s compared to 3.76 mm/s for the layer reinforced with a geogrid placed at a depth of 250 mm.

The velocity profiles of ballast assemblies reinforced with geogrids placed at shallower depths (150 mm, 100 mm, and 50 mm) are markedly different from the previously mentioned layers. In the stable zone, particle velocities remain almost constant up to around 150 mm across all three layers. However, in the active zone, the increase in particle velocity is less pronounced than in both the unreinforced layer and layers with geogrids placed at depths of 200 mm and 250 mm. The layers with geogrids at 100 mm and 150 mm shown similar velocity increases, with maximum velocities of 2.00 mm/s and 1.76 mm/s respectively occurring near the top. The layer with a geogrid situated 50 mm under the tie exhibits only slight increases in velocity in the active zone, reaching a peak of 0.97 mm/s. This reduced velocity





(a)



(b)

Fig. 12 a Variation of the average particle velocity with depth as a function of the geogrid placement depth and b effect of the geogrid location on the variation of average particle angular velocity with depth

increase in the active zone for ballast layers with geogrids at depths of 50 mm, 100 mm, and 150 mm indicates the effectiveness of geosynthetics in stabilizing the ballast aggregate, preventing its excessive displacement and thereby minimizing the resulting tie settlement.

The inclusion of geogrids in the ballast assemblies impacts the rotational motion of ballast particles. Fig. 12b presents the evolution of the average angular velocity of ballast particles along the height of each layer. In the unreinforced ballast layer, a noticeable uptick in angular velocity starts at a height of 125 mm, escalating sharply in the active zone. Ballast layers with geogrids located at depths of 200 mm and 250 mm exhibit similar patterns with relatively constant angular velocities in the stable zone following by a rapid increase with height in the active zone. Peak angular velocities in the unreinforced layer and those reinforced with geogrids at 250 mm and 200 mm reach 0.22 rad/s, 0.16 rad/s, and 0.23 rad/s, respectively.

On the other hand, ballast layers with geogrids at 150 mm, 100 mm, and 50 mm demonstrate considerably lower angular velocities. These layers maintain nearly uniform angular velocities in the stable zone. In the active zone, the layers with geogrids at 150 mm and 100 mm display similar trends of angular velocity increase, reaching maximums of 0.09 rad/s and 0.11 rad/s respectively. The layer with a geogrid placed 50 mm beneath the tie shows the smallest increase in angular velocity within the active zone, peaking at 0.05 rad/s. This indicates a more pronounced effect of geogrids at shallower depths in mitigating the rotational motion of ballast particles.

### 4.2.3 Contact Force Chains

Under cyclic loading, ballast particles reorganize to bear the applied loads, transmitting forces via interparticle contacts that create a complex network for force chains. As Radjai et al. (1997, 1998) and Thornton and Antony (1998) stated, these contacts may be divided into two subnetworks: a strong network with forces ( $F_c$ ) larger than the average contact force ( $\overline{F_c}$ ) and a weak contact network carrying forces smaller than the average contact force. The strong contact network, mainly aligned with the deviator stress direction, consists of continuous force chains that provide the bulk of the soil's shear strength (Lai et al. 2014; Y. Liu & Yan 2023). Conversely, the weak network forces are usually perpendicular to the strong network and support the stability of strong force chains (J. Liu et al. 2020; Minh et al. 2014). Chen et al. (2022a, b) further classified the strong contact network in geogrid-reinforced soils under monotonic loading into three types: type I ( $\overline{F_c} \leq F_c < 2\overline{F_c}$ ), type II ( $2\overline{F_c} \leq F_c < 3\overline{F_c}$ ), and type III ( $F_c \geq 3\overline{F_c}$ ), noting that type III contacts play an important role in stress dispersion and load transfer, both vertically to the soil's support and horizontally to type I and II contacts (J. Chen, Bao, et al. 2022a, b).

Fig. 13 a to f depict the contact force networks in both unreinforced and geogrid-reinforced ballast layers during the 20th load cycle. Contact forces are represented by cylinders, with thicker ones indicating greater forces. Each network comprises a weak contact network and three strong contact subnetworks (types I, II, and III) based on the classification proposed by Chen et al. (2022a, b). Across all samples, type III forces exhibit a primarily vertical orientation and are located beneath the

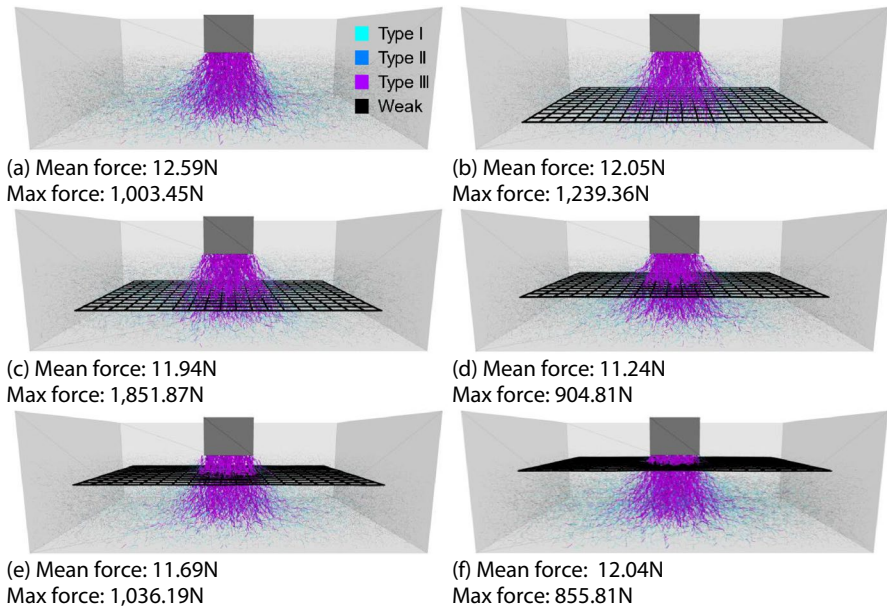


**Fig. 13** Contact force chains during the 20th load cycle in **a** unreinforced and reinforced ballast layers with a geogrid located at a depth of **b** 250 mm, **c** 200 mm, **d** 150 mm, **e** 100 mm, and **f** 50 mm

tie, correlating with the direction of the applied compressive load. Meanwhile, type I and II contacts are oriented more laterally, consistent with Chen et al.'s findings. The unreinforced ballast layer exhibits the highest mean contact force of 12.59 N, while the incorporation of geogrids generally reduces the average contact force, with the lowest one being recorded in the layer reinforced with a geogrid at a depth of 150 mm.

The impact of the geogrid placement depth on the average type III contact force within select ballast layers is examined in Fig. 14. For clarity, the figure only includes the contact force variations of the unreinforced ballast layer and layers with geogrids positioned at depths of 250 mm, 150 mm, and 50 mm. The unreinforced layer exhibits the greatest average type III contact forces throughout its entire height, ranging from 139.14 N at the bottom to 245.13 N at the top. Adding a geogrid reduces these contact forces, with deeper placement depths (e.g., 250 mm) resulting in smaller force reductions. On the other hand, shallower placement depths of 150 mm and 50 mm show more significant decreases in average contact forces. This finding reflects the effect of the geogrid location of the geogrid-induced reductions in tie settlement and particle velocity observed in Figs. 9b and 12a and b.

The forces transmitted at interparticle contacts are affected by the ballast layer's microstructure and its number of contacts. The number of contacts per particle in a granular assembly is described by the coordination number (CN) which gives a measure of the average number of contacts per particle and packing intensity at the particle level. It is defined as  $CN = 2N_c/N_p$  where  $N_c$  is the number of contacts in the granular system and  $N_p$  is the number of particles (O'Sullivan 2011). The

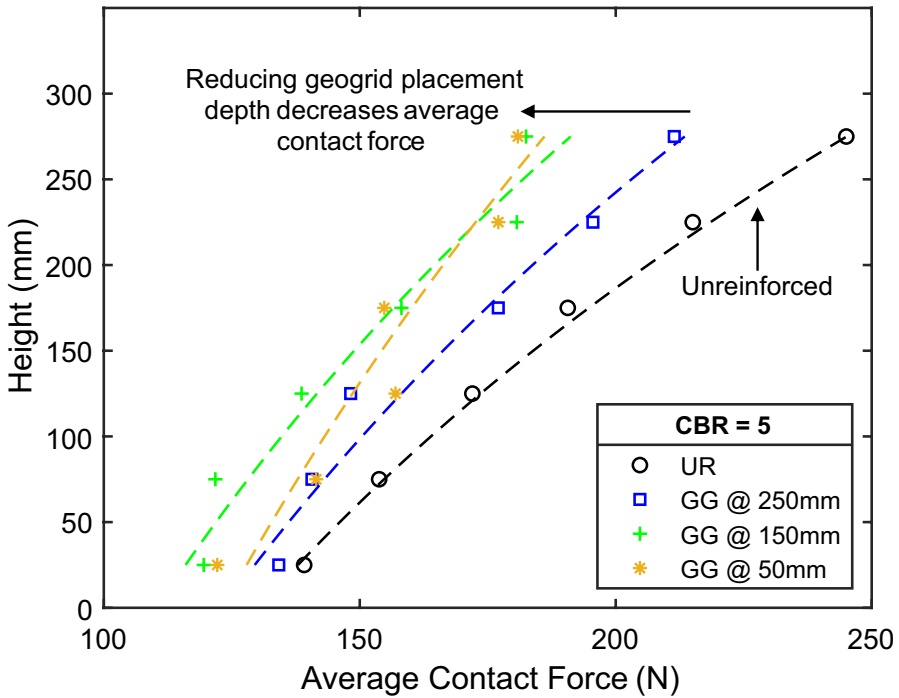


**Fig. 14** Effect of geogrid placement depth on the variations in average contact force among type III contacts in unreinforced and geogrid-reinforced ballast assemblies

coordination number affects the macroscopic behavior and stability of granular materials, with a high coordination number being associated with an increased stability and stiffness, enhanced load transfer ability, and reduced potential for particle breakage (Fei & Narsilio 2020; Gu et al. 2014; Luo, Zhao, Bian, et al. 2023a, b; Minh & Cheng 2013; O’Sullivan 2011; Ouadfel 1998).

Figure 15 tracks the changes in coordination number across all ballast samples during cyclic loading. A common pattern emerges, whereby each layer shows a marked reduction in its coordination number after the first load cycle followed by a gradually decreasing reduction with successive load cycles. The unreinforced layer possesses the lowest coordination number and experience a sustained reduction of its CN during cyclic loading, indicating a weaker particle interconnectivity. This translates into a more deformable soil structure and results in the emergence of higher interparticle contact forces as evidenced by the data plotted in Fig. 14. By the end of cyclic loading, its coordination number reaches a value of 6.36. In contrast, ballast assemblies with geogrids at depths of 250 mm and 200 mm exhibit smaller CN decreases than their unreinforced counterpart. Their initial sharp decline in CN transitions to gradual reductions, ending with a CN of 6.55 in both layers.

The CN values further reflect the efficacy of geogrids at depths of 150 mm and above. Ballast layers with geogrids positioned 150 mm, 100 mm, and 50 mm beneath the tie display minimal changes in their coordination number, reaching final

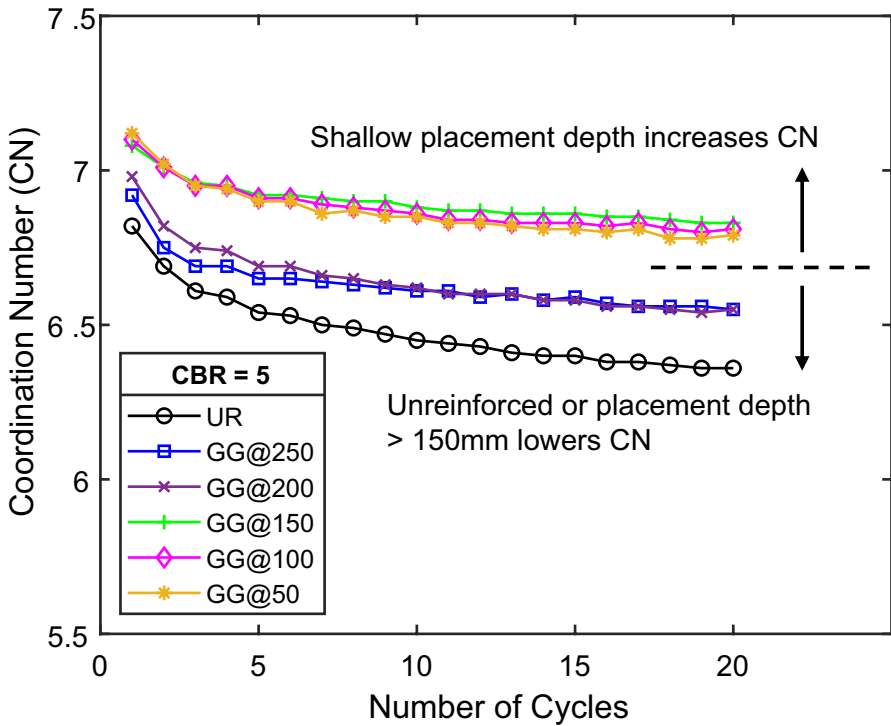


Fig. 15 Evolution of the coordination number during cyclic loading in unreinforced and geogrid-reinforced ballast layers

values of 6.78, 6.76, and 6.74, respectively. These higher coordination numbers suggest enhanced particle connectivity, leading to a more stable and stiffer soil structure. Consequently, these layers are more resistant to the applied loads and exhibit reduced interparticle forces (Fig. 14), potentially indicating a reduced potential for particle breakage.

#### 4.2.4 Energy Dissipation

Applying a cyclic compressive load to a ballast assembly through a tie is a process that involves the storage, transformation, and dissipation of energy. External energy is input into the system through the motion of the tie. This energy is then transformed into mechanical energy ( $E_m$ ), which is a combination of mechanical body energy ( $E_{mb}$ ) and mechanical contact energy ( $E_{mc}$ ) expressed as follows (J. Chen, Bao, et al. 2022a, b):

$$E_m = E_{mb} + E_{mc} \tag{29}$$

$$E_{mb} = E_{pot} + E_{kin} + E_{damp} \tag{30}$$

$$E_{mc} = E_k + E_\mu + \overline{E_k} \quad (31)$$

where  $E_{pot}$  is the potential energy,  $E_{kin}$  is the kinetic energy,  $E_{damp}$  is the energy dissipated by non-viscous damping,  $E_k$  is the strain energy stored in the linear springs,  $E_\mu$  is the energy dissipated by frictional slip, and  $\overline{E_k}$  is the strain energy stored in the parallel bond springs (applicable to models where geogrids are present).

In the discrete element simulations presented in this paper, energy dissipation may occur through non-viscous damping and interparticle frictional sliding once the contact's frictional strength is exceeded. To investigate the effect of geogrids on the dissipation of energy at the contact level, the cumulative energy dissipated through frictional slip is tracked during the simulations. The energy dissipated by frictional slip  $E_\mu$  is expressed as follows:

$$E_\mu = E_\mu - \frac{1}{2}((F_s^l)_0 + (F_s^l)) \cdot \Delta\delta_s^\mu \quad (32)$$

where:

$$\Delta\delta_s^\mu = \Delta\delta_s - \Delta\delta_s^k = \Delta\delta_s - \left( \frac{F_s^l - (F_s^l)_0}{k_s} \right) \quad (33)$$

And  $(F_s^l)_0$  is the linear shear force at the beginning of the timestep,  $\Delta\delta_s$  is the adjusted relative shear displacement increment, and  $\Delta\delta_s^k$  and  $\Delta\delta_s^\mu$  are the shear displacement's elastic and slip component, respectively.

The cumulative energy dissipated through frictional slip in the unreinforced ballast layer and ballast beds reinforced with geogrids located at depths of 150 mm, 100 mm, and 50 mm is illustrated in Fig. 16. Although a similar amount of energy is dissipated in all ballast layers during the first load cycle, the unreinforced ballast layer experiences a sustained growth in the energy dissipated through interparticle sliding during the 20 load cycles, reaching a total of 162.33 J at the end of the ballast box test. The ballast assemblies reinforced with geogrids located in the layers' upper 150-mm display reduced tendencies to dissipate energy through frictional sliding. This is attributed to their better-connected soil structure and the confining effects of the geogrids, which effectively restrains particle movement. Following the first load cycle, the reinforced layers register gradually smaller increases in energy dissipated through frictional slip under additional cyclic loading. At the end of the text, the total energy dissipated in the layers reinforced with geogrids located 150 mm, 100 mm, and 50 mm beneath the tie amount to 102.33 J, 105.76 J, and 107.63 J, respectively. It is noteworthy that although the results for the ballast layers reinforced with geogrids positioned 250 mm and 200 mm below the tie are not presented in Fig. 16 for brevity, a total of 135.13 J and 139.31 J respectively is dissipated in each layer, providing an intermediate performance compared to the layers where geogrids are placed closer to the tie.

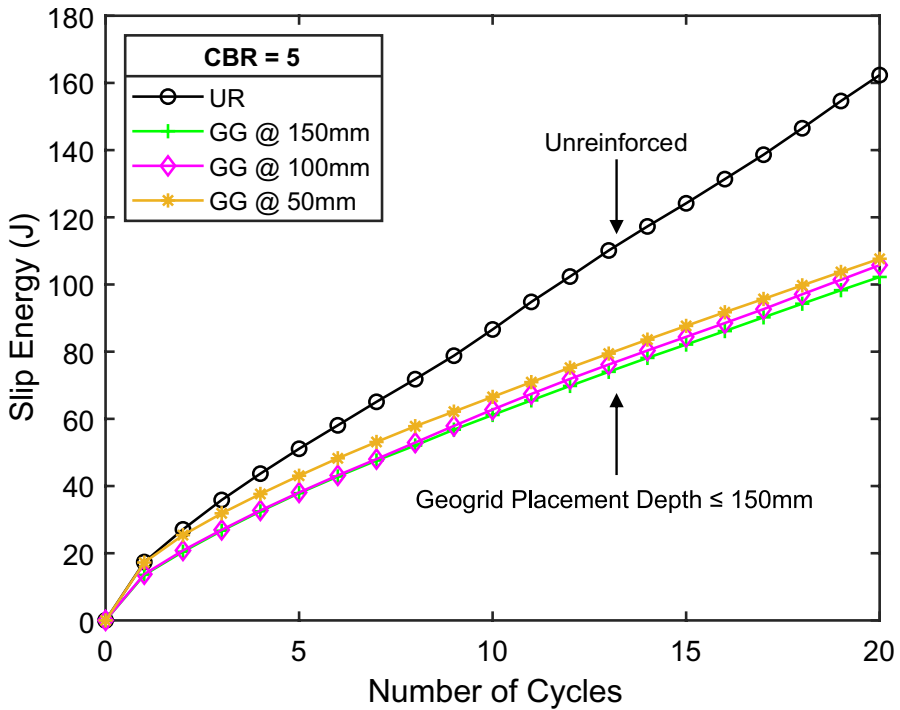
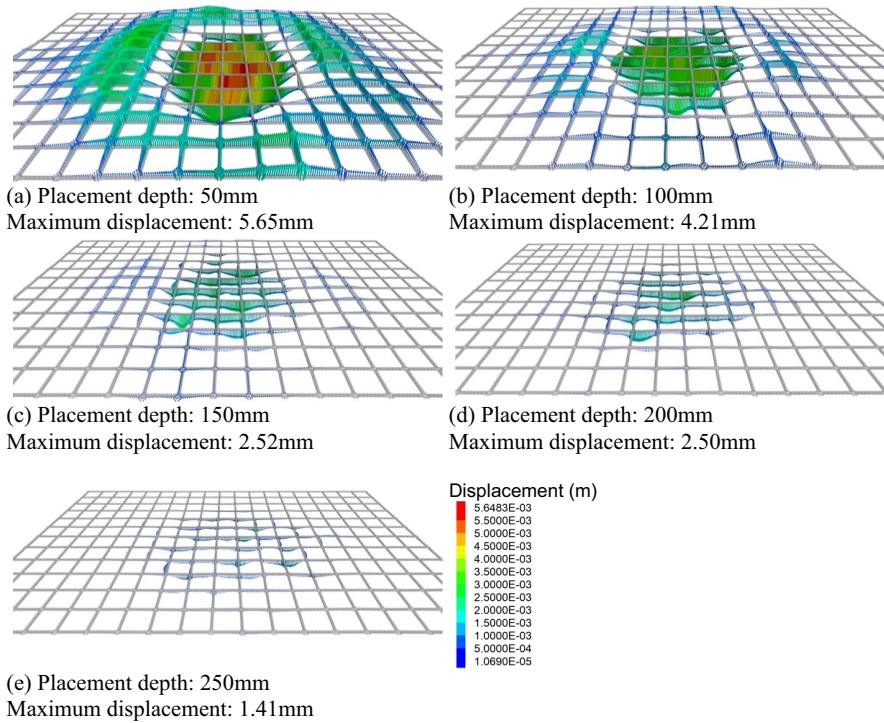


Fig. 16 Energy dissipated by frictional sliding in the unreinforced and reinforced ballast layers with geogrids located at depths of 150 mm, 100 mm, and 50 mm

### 4.3 Geogrid Response

The deformation profiles of geogrids at various depths in ballast layers during the application of the 20th load cycle are plotted in Fig. 17a to e. The geogrid positioned 50 mm below the tie (Fig. 17a) exhibits the most notable deformation, characterized by a significant depression at its center directly beneath the tie. This depression aligns with the downward movement of ballast particles observed under the tie as shown in Fig. 11. In contrast, the ribs surrounding the central area of the geogrid exhibit upward movement, which is consistent with the displacement of ballast aggregates adjacent to the tie. As the geogrid placement depth increases (100 mm, 150 mm, 200 mm, and 250 mm in Fig. 17b to e), the central depression beneath the tie decreases in magnitude. It is noteworthy that the ribs surrounding the centrally depressed area of the grid shift from an upward to a lateral displacement pattern. Additionally, the geogrids placed 200 mm and 250 mm beneath the tie show markedly reduced deflections, indicating a lesser degree of reinforcement mobilization compared to shallower geogrids.

The deformation of each geogrid causes strain energy ( $E_k$ ) to be stored in the parallel-bonded contacts linking the spheres that make up each reinforcement. The parallel bond strain energy is given by the following:



**Fig. 17** Total displacement vectors (in meters) of the parallel-bonded balls drawn at the same scale for the geogrids placed at depths of **a** 50 mm, **b** 100 mm, **c** 150 mm, **d** 200 mm, and **e** 250 mm

$$\bar{E}_k = \frac{1}{2} \left( \frac{\bar{F}_n^2}{k_n A} + \frac{\|\bar{\mathbf{F}}_s\|^2}{k_s A} + \frac{\bar{M}_t^2}{k_t J} + \frac{\|\bar{\mathbf{M}}_b\|^2}{k_n \bar{I}} \right) \quad (34)$$

where  $\bar{F}_n$  and  $\bar{F}_s$  are the normal and shear components of the parallel-bond force,  $\bar{M}_t$  and  $\bar{M}_b$  are the twisting and bending moment components of the parallel-bond moment, and  $\bar{I}$  and  $\bar{J}$  are the moment of inertia and polar moment of inertia of the parallel bond cross section, respectively.

The parallel bond strain energy is tracked during the application of cyclic loading to each geogrid-reinforced ballast assembly to provide a scalar index of the load being carried by each geogrid. The evolution of the parallel bond strain energy of each geogrid is plotted in Fig. 18. The geogrid located 50 mm beneath the tie stores the most strain energy, a consequence of its proximity to the loaded area and the substantial displacement of its ribs. After the initial load cycle, this geogrid carries 37% of the strain energy it stored during the 20th load cycle which amounts to 2.60 J. This is a marked difference compared to the strain energies stored in the other geogrids.

In the initial phases of loading, the geogrids positioned 100 mm and 150 mm below the tie show similar magnitudes of stored strain energy. However, as cyclic



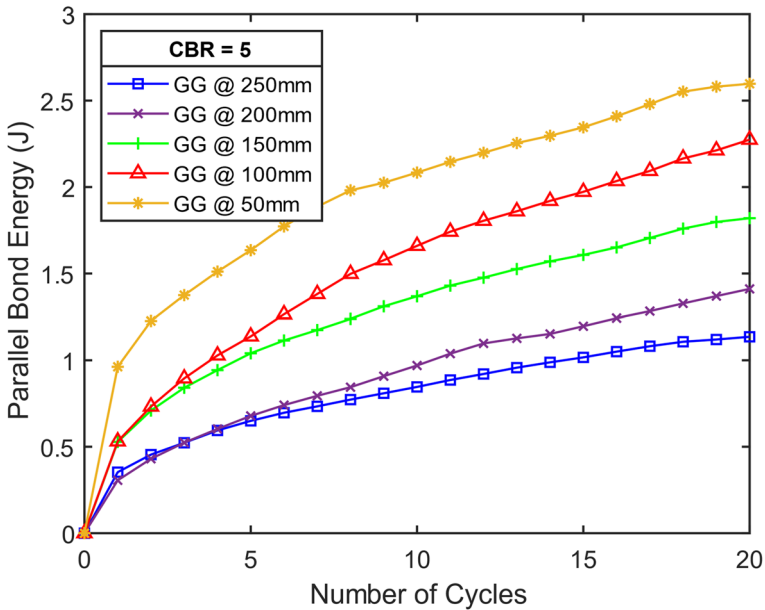


Fig. 18 Accumulation of strain energy stored in the geogrid’s parallel bond springs during cyclic loading

loading progresses, the geogrid at 100 mm demonstrates a continuous increase in stored strain energy, surpassing that of the 150-mm geogrid. By the 20th load cycle, the strain energies stored in these geogrids are 2.27 J and 1.82 J, respectively. Reflecting their respective deformation profiles, the geogrids situated deeper in the ballast layer at depths of 200 mm and 250 mm store significantly lower magnitudes of strain energy. These two geogrids exhibit comparable amounts of stored strain energy until the fifth load cycle. Beyond this point, the geogrid at 200 mm begins to store more strain energy than its counterpart at 250 mm, finishing the cyclic load tests with strain energies of 1.41 J and 1.14 J, respectively.

This analysis of strain energy storage aligns with the deformation profiles observed in each geogrid and highlights the relationship between the geogrid placement depth and its ability to stabilize railroad ballast. The decrease in strain energy stored in the geogrids’ parallel bonds with increasing depth underscores the diminishing mobilization of reinforcements placed deeper in the ballast layer.

### 5 Parametric Study

Simulating the behavior of geogrid-reinforced ballast layers subjected to cyclic loading where geogrids are placed at depths ranging from 50 to 250 mm beneath the tie demonstrates that ballast particles that are the most disturbed by the application of cyclic loading are overwhelmingly located within the upper 150mm of the ballast bed. Correspondingly, geogrids situated within the upper half of the 300-mm-thick ballast layers exhibit superior tie settlement-abating abilities due

to the formation of an interlock with the surrounding aggregates that restrains particle motion and creates a well-connected soil structure.

Although geogrids located 50 mm and 100 mm beneath the tie perform their reinforcing functions satisfactorily, their placement depths are not practically desirable in the context of ballasted railway substructures as they would interfere with common ballast maintenance operations such as tamping. As such, in the framework of the simulations discussed herein, the optimum geogrid placement depth is set at 150 mm below the base of the tie to achieve the maximum reduction in tie settlement while simultaneously being practically feasible.

To explore in-depth the parameters that influence the behavior of geogrid-reinforced ballast, a parametric study is conducted in which the geogrid stiffness and geogrid aperture size are varied. In both cases, the geogrid placement depth is kept constant at 150 mm. The geogrid stiffness is changed to represent the biaxial geogrid's tensile strength at 2% strain at temperatures of  $-30$ ,  $-10$ ,  $10$ ,  $20$ , and  $40$  °C reported by Desbrousses et al. (2021). The effect of the geogrid's aperture size ratio is also investigated by varying the aperture size ( $A$ ) to  $30 \times 30$ mm,  $40 \times 40$ mm,  $50 \times 50$ mm,  $57 \times 57$ mm,  $70 \times 70$ mm, and  $80 \times 80$ mm, while keeping the geogrid's tensile strength at 2% strain constant. When divided by the ballast particle's diameter ( $D$ ) of 27.5 mm, the aperture sizes give aperture size ratios ( $A/D$ ) of 1.09, 1.45, 1.82, 2.07, 2.55, and 2.91.

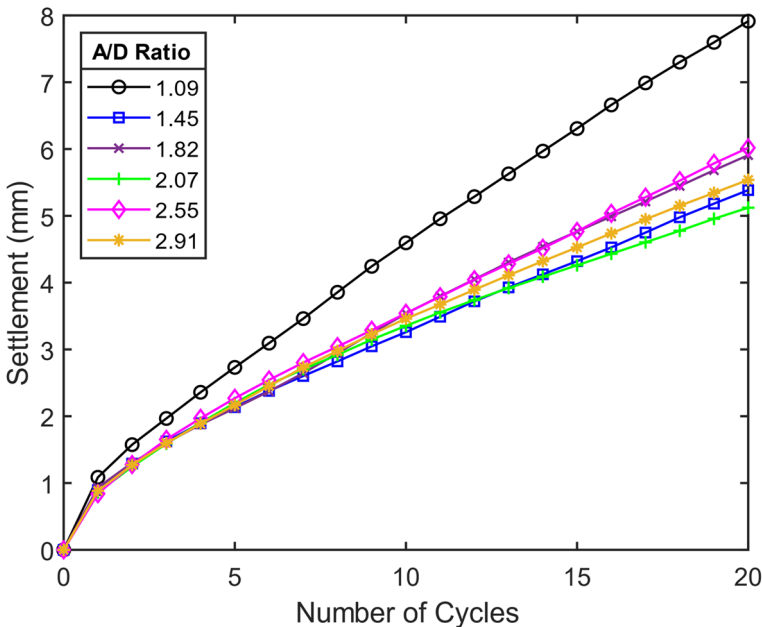


**Fig. 19** Effect of the geogrid aperture size ratio ( $A/D$ ) on the evolution of the tie settlement in ballast layers reinforced with a geogrid located 150mm beneath the tie

## 5.1 Effect of Geogrid Aperture Size Ratio

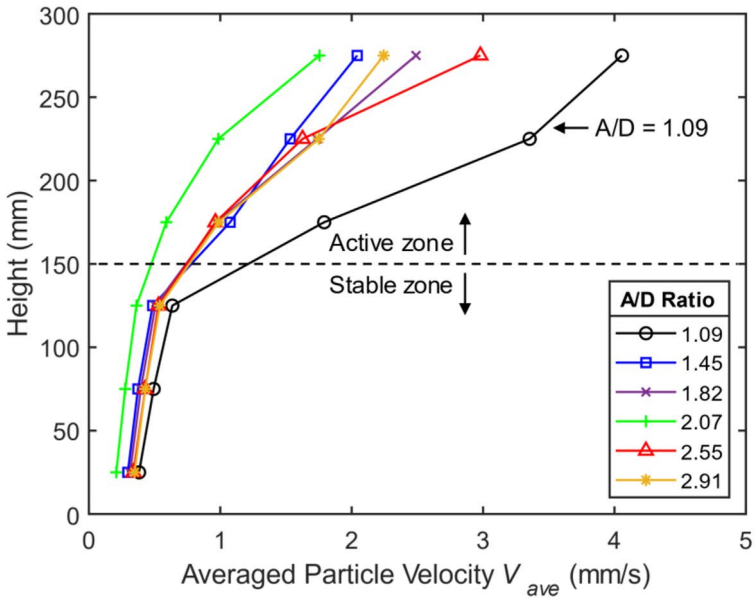
Figure 19 shows the effect of the geogrid aperture size on the accumulation of tie settlement during 20 load cycles in ballast layers reinforced with geogrids placed 150 mm beneath the tie with aperture size ratios ranging from 1.09 to 2.91. A geogrid with an  $A/D$  of 1.09 results in considerable tie settlement, reaching 7.91 mm after 20 load cycles. This is significantly higher than the 5.12-mm settlement observed with the original 57-mm geogrid ( $A/D = 2.07$ ) and is comparable to the tie settlement in the unreinforced ballast bed (see Fig. 9b). Incrementally increasing the aperture size ratio to 1.45 reduces tie settlement by 32%, achieving a final subsidence of 5.38 mm. Further increasing  $A/D$  to 1.82 results in a slightly higher tie settlement of 5.91 mm. The lowest tie settlement recorded is with the original 57 mm aperture geogrid ( $A/D = 2.07$ ). Increasing the  $A/D$  ratio to 2.55 and 2.91 results in gradual increases in tie settlement, with final values of 6.02 mm and 5.54 mm, respectively.

To delve into the micromechanical implications of changing the geogrid opening size, the variations in particle translational and rotational velocity with depth along the ballast layer are plotted in Fig. 20a and b respectively. Both figures stress the inadequacy of an  $A/D$  ratio of 1.09, as evidenced by the sharp increases in both translational and angular velocities of ballast particles that take place around the geogrid's location. This suggests that the geogrid's small opening size hinders the formation of a stable interlock with the surrounding ballast, which splits the layer into two halves and promotes excessive particle rotation and translation above the geogrid. In contrast,  $A/D$  of 1.45 and up lead to marked reductions in both particle velocities, indicating a more effective stabilization of the ballast and a correspondingly lower tie settlement.

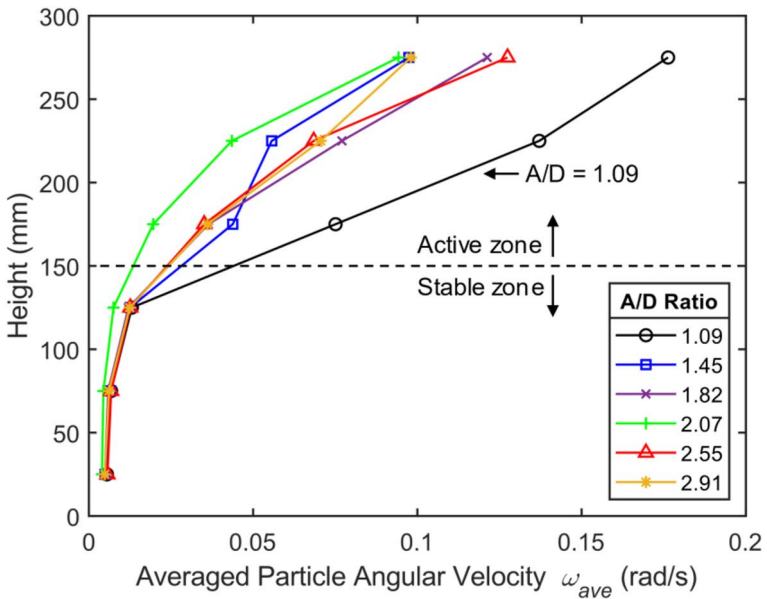
Figure 21, which displays the tie plotted settlement against aperture size, corroborates the findings presented in this subsection. The 30-mm aperture geogrid is deemed unsuitable for reinforcing the simulated ballast due to its small opening size. However, apertures ranging from 40 to 80 mm demonstrate satisfactory performance. The observed trend suggests that an aperture size of approximately 60 mm ( $A/D$  of 2.18) could be optimal for minimizing tie settlement in the context of the mono-sized ballast particles considered in the simulations.

## 5.2 Effect of Geogrid Stiffness

The effect of changing geogrid stiffness is investigated by simulating geogrids with a tensile strength at 2% strain that matches the values recorded by Desbrousses et al. (2021, 2023a) when performing tensile tests on samples of the biaxial geogrid at temperatures of  $-30$ ,  $-10$ ,  $10$ ,  $20$ , and  $40$  °C. This tensile strength variation aims to understand the influence of geogrid stiffness on tie settlement, energy dissipation by frictional sliding, and the strain energy stored in the geogrids' parallel bond springs. The geogrids are all embedded in the ballast layers at a depth of 150 mm below the tie. Table 5 summarizes the findings for total tie settlement, cumulative slip energy, and parallel bond strain energy for each geogrid stiffness during the 20th load cycle.



(a)



(b)

**Fig. 20** Effect of the geogrid aperture size ratio ( $A/D$ ) on the (a) average particle velocity and (b) average particle angular velocity

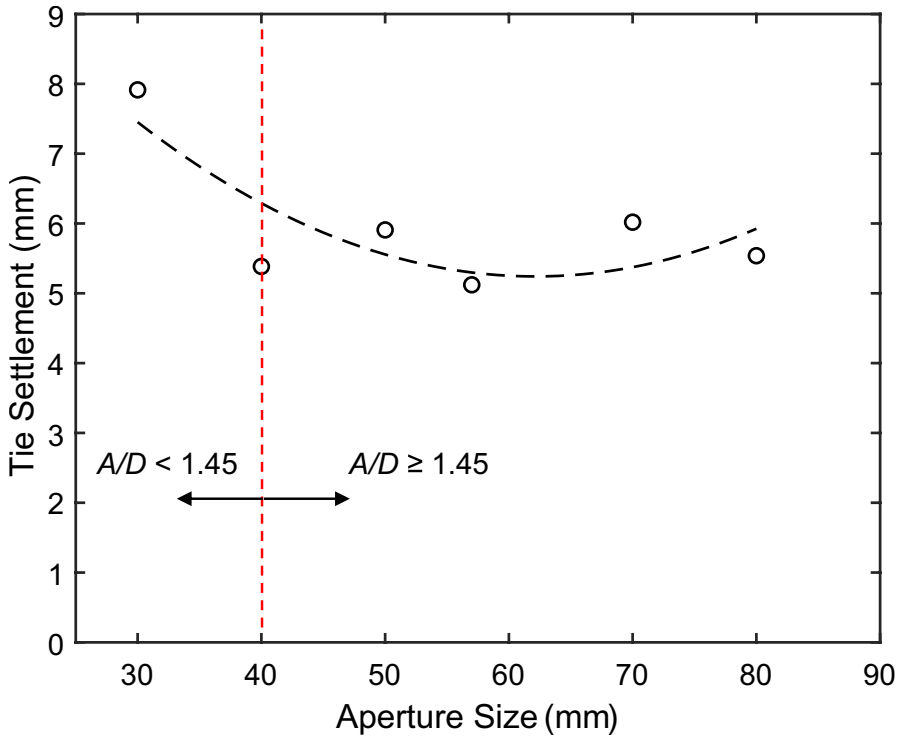


Fig. 21 Optimum size of the geogrid’s apertures based on total tie settlement considerations

Table 5 Effect of geogrid stiffness on the tie settlement, energy dissipated by frictional sliding, and parallel bond strain energy after 20 load cycles

Temperature (°C)	-30	-10	10	20	40
Geogrid stiffness (kN/m)	18.00	16.28	14.61	11.01	9.54
Tensile modulus at 2% strain (kN/m)	900	814	730.5	550.5	477
Settlement (mm)	5.13	4.96	4.90	5.12	5.14
Slip energy (J)	100.95	100.22	98.72	102.24	102.38
Bond strain energy (J)	1.52	1.61	1.69	1.82	1.94

The results indicate a relative insensitivity of the tie settlement to the geogrid’s tensile strength at 2% strain. Tie subsidence values of 5.13 mm, 4.96 mm, 4.90 mm, 5.12 mm, and 5.14 mm are recorded for geogrid stiffnesses of 18.00 kN/m, 16.28 kN/m, 14.61 kN/m, 11.01 kN/m, and 9.54 kN/m, respectively. This is supported by the consistency of cumulative energy dissipated by frictional slip across samples reinforced with geogrids of different stiffnesses, with values ranging narrowly between 98.72 and 102.38 J.

In contrast, the strain energy stored in the geogrids’ parallel bond springs is markedly dependent on the geosynthetic’s tensile strength at 2% strain. The greatest

amount of strain energy is observed in geogrids with the lowest stiffnesses, as they offer the least resistance to deformation. Consequently, the highest bond strain energy during the 20th load cycle is recorded in the geogrid with a stiffness of 9.54kN/m, while the lowest is associated with the geogrid having a stiffness of 18.00 kN/m.

## 6 Discussion

In the previous sections, the results illustrate the influence of geogrid placement depth, aperture size ratio, and stiffness on the deformation behavior of geogrid-reinforced ballast subjected to cyclic loading. Geogrids positioned at depths ranging from 50 to 150 mm yield the most significant reductions in tie settlement, which is attributed to their ability to confine ballast particles through the development of a geogrid-ballast interlock. This confinement leads to reduced particle movement and total slip energy, along with an increase in the average coordination number, indicating more interconnected soil structures. However, the efficacy of geogrid reinforcement wanes at greater placement depths (200 and 250 mm), resulting in increased tie settlements, more pronounced particle movement, and lower coordination numbers.

Further analysis reveals that the aperture size of geogrids is critical for the effective reinforcement of the mono-sized ballast (diameter of  $D = 27.5\text{mm}$ ) considered in the simulations. An aperture size ( $A$ ) of  $30 \times 30 \text{ mm}$  ( $A/D = 1.09$ ) proves too small and impedes the formation of a stable ballast-geogrid interlock. This contributes to the formation of a displacement plane at the geogrid level that splits the ballast layer in two, with substantial particle movement occurring above the geogrid. Optimal tie settlement reduction is observed for  $A/D$  ratios greater than or equal to 1.45. Interestingly, variations in geogrid stiffness, ranging from a tensile strength at 2% strain of 18.00 to 9.54kN/m, have a lesser impact on ballast reinforcement compared to the aperture size, with similar tie settlement outcomes across the stiffness range.

Studies summarized in Table 6 explored the impact of geogrid placement depth and aperture size on the performance of geogrid-reinforced ballast. Cyclic load tests conducted on geogrid-reinforced ballast (Bathurst et al. 1986; Bathurst & Raymond 1987; C. Chen et al. 2012; Desbrousses et al. 2023; Indraratna et al. 2013) have indicated that geogrids placed closer to the bottom of the ties are more effective at reducing tie settlement. Guidelines on the use of geogrids for ballast reinforcement provided by AREMA (2010) further state that geogrids may be placed within the ballast layer to reduce the rate of track settlement. This aligns with the findings presented in this paper which demonstrate notable settlement reductions with geogrids positioned within the upper 150 mm of the ballast layer. It is important to note that it is generally advised to place geogrids at a depth of at least 150 mm below the tie (Das 2016) to prevent interference with common ballast maintenance operations such as tamping, which tend to disturb the upper 100 mm of the ballast layer (Bathurst & Raymond 1987; Guo et al. 2021; Offenbacher et al. 2021; S. Shi et al. 2022).

**Table 6** Summary of studies investigating the effect of geogrid placement depth and aperture size

Author(s)	Experiment	Ballast thickness	Geogrid depth mm	Geogrid aperture size	Optimum depth	Optimum aperture	Observations
Bathurst et al. (1986, 1987)	Ballast box test	300 mm	50, 100, 150, 200 mm	46 × 46 mm	200 mm	N/A	<ul style="list-style-type: none"> <li>- Minimum tie settlement at geogrid depths of 50 and 100 mm</li> <li>- Preferred placement depth at 200 mm due to practical considerations</li> </ul>
McDowell and Stickley (2006)	Ballast box test	300 mm	100, 200 mm	39 × 39 mm, 65 × 65 mm	200 mm	65 mm	<ul style="list-style-type: none"> <li>- Smaller tie settlement is obtained with a geogrid aperture size of 65 mm and a depth of 200 mm.</li> </ul>
McDowell et al. (2006)	Pullout test (DEM)	N/A	N/A	$A/D_{50}$ 0.9, 1.1, 1.4, 1.6	N/A	$A/D_{50}$ 1.4	<ul style="list-style-type: none"> <li>- Lowest pullout resistance for <math>A/D_{50}</math> 0.9</li> <li>- Maximum pullout force for <math>A/D_{50}</math> 1.4</li> <li>- Similar pullout forces for <math>1.1 &lt; A/D_{50} &lt; 1.6</math></li> </ul>
Brown et al. (2007)	Ballast box test	300 mm	250 mm	$A/D_{50}$ 0.64, 0.76, 1, 1.3, 1.8, 2	N/A	$A/D_{50}$ 1.2–1.6	<ul style="list-style-type: none"> <li>- Shear plane develops at the geogrid level if apertures are too small.</li> </ul>

Table 6 (continued)

Author(s)	Experiment	Ballast thickness	Geogrid depth	Geogrid aperture size	Optimum depth	Optimum aperture	Observations
Indraratna et al. (2013), Hussaini et al. (2015, 2016)	Process simulation test	325 mm	130, 195, 265, 325 mm	$A/D_{50}$ 0.6, 1.08, 1.21, 1.85	265 mm	$A/D_{50}$ 1.21	<ul style="list-style-type: none"> <li>- Geogrids reduce ballast breakage and lateral spreading.</li> <li>- Geogrids with <math>A/D_{50} &gt; 0.95</math> are suitable for reinforcing ballast.</li> <li>- Optimum geogrid location is 65 mm above subballast.</li> </ul>
Chen et al. (2013, 2014)	Pullout test	N/A	N/A	32, 40, 65, 75 mm	N/A	65 mm	<ul style="list-style-type: none"> <li>- Geogrid aperture size is more influential than geogrid stiffness and rib thickness for geogrid-ballast interlock.</li> <li>- Triangular geogrid is better at interacting and confining ballast.</li> <li>- Small geogrid apertures prevent interlocking.</li> </ul>



Table 6 (continued)

Author(s)	Experiment	Ballast thickness	Geogrid depth	Geogrid aperture size	Optimum depth	Optimum aperture	Observations
Chen et al. (2012)	Ballast box test (DEM)	300 mm	50, 100, 150, 200, 250 mm	65 mm	200 mm	N/A	<ul style="list-style-type: none"> <li>- Best depth of the geogrid is 100 mm followed by 150 and 200 mm.</li> <li>- Triangular grid interlock better with ballast</li> <li>- Resilient behavior is not affected by presence of geogrid.</li> </ul>
Hussaini and Sweta (2020, 2021); Sweta and Hussaini (2018, 2020, 2022)	Process simulation test Direct shear test	380 mm	Ballast/subballast interface	$A/D_{50}$ 0.63, 0.83, 0.93, 0.95, 1.54	N/A	$A/D_{50}$ 0.93	<ul style="list-style-type: none"> <li>- The role of aperture size is striking around the geogrid location in terms of lateral spreading.</li> <li>- Recommended aperture sizes suitable for geogrid at ballast/subballast interface</li> </ul>
Esmaeili et al. (2017)	Single-tie push test Track panel displacement test	450 mm	250, 350 mm	40 × 40 mm	250 mm	N/A	<ul style="list-style-type: none"> <li>- Increase in lateral track resistance caused by geogrid decreases with increasing geogrid placement depth.</li> </ul>

Table 6 (continued)

Author(s)	Experiment	Ballast thickness	Geogrid depth	Geogrid aperture size	Optimum depth	Optimum aperture	Observations
Sadeghi et al. (2020, 2023)	Direct shear test Ballast box test	450 mm	250, 350 mm	$A/D_{50}$ 0.83, 1.17, 1.59	350 mm	$A/D_{50}$ 1.17	- $A/D_{50}$ 1.17 with a placement depth of 200 mm yields optimum reinforcement in sand-fouled ballast giving a stiffer layer, with less settlement and particle breakage. - $A/D_{50}$ 1.17 increases ballast's shear strength in direct shear test due to superior interlock with ballast.
Indraratna et al. (2020)	Impact test	300 mm	100, 200, 300 mm	$A/D_{50}$ 1.2	200 mm	N/A	- Maximum reduction in ballast axial and radial strain achieved by geogrid placed 100 mm above subballast - Maximum reduction in ballast breakage achieved by geogrid placed at a depth of 100 mm

**Table 6** (continued)

Author(s)	Experiment	Ballast thickness	Geogrid depth	Geogrid aperture size	Optimum depth	Optimum aperture	Observations
Li et al. (2024)	Impact test	400 mm	300, 350 mm	$A/D_{50}$ 1.4	300 mm	N/A	- Optimum geogrid placement depth is 100 mm above sub-ballast to minimize axial and lateral ballast deformations.

The role of the geogrid aperture size in enhancing ballast reinforcement has been investigated through various testing methods, including direct shear tests (Indraratna et al. 2011, 2012; Sadeghi et al. 2020; Sweta & Hussaini 2018), pullout tests (C. Chen et al. 2013), triaxial tests (Mishra et al. 2014; Qian et al. 2015), and variants of the ballast box tests (Hussaini et al. 2015, 2016; Indraratna et al. 2013; Sadeghi et al. 2023). Indraratna et al. (2012, 2013) and Hussaini et al. (2015, 2016) studied the effect of the  $A/D_{50}$  ratio between a geogrid's aperture size ( $A$ ) and the ballast's mean particle diameter ( $D_{50}$ ) using direct shear tests and cyclic load tests on the behavior of geogrid-reinforced ballast. They reported that optimum geogrid reinforcement is achieved for  $A/D_{50}$  ratios ranging from 0.95 to 1.20, while acceptable reinforcement exists for ratios in excess of 1.20. Other studies, such as the cyclic load tests performed by Brown et al. (2007) and the pullout tests conducted by Chen et al. (2013), recommend using greater  $A/D_{50}$  ratios in the range of 1.2 to 1.6 for optimal reinforcement. On the other hand, AREMA (2010) indicates that using geogrids with an aperture size in excess of 43 mm results in optimal geogrid performance, irrespective of the ballast particle size. The results drawn from the simulations discussed herein echo the findings of Brown et al. (2007) and AREMA's recommendations (AREMA 2010) by demonstrating effective geogrid performance for aperture size ratios greater than 1.45.

Regarding the geogrid stiffness, AREMA recommends using geogrids with a minimum tensile modulus at 2% strain of  $277 \times 474$  kN/m (machine  $\times$  cross-machine directions) for adequate performance in railroad ballast. Brown et al. (2007) further stated that increasing geogrid stiffness leads to better ballast reinforcement provided that sufficient overburden pressure exists above the geosynthetic. The parametric study presented in this paper is consistent with the AREMA guidelines, suggesting that adequate geogrid performance is achieved with geogrid tensile moduli at 2% strain in excess of 474 kN/m.

## 7 Limitations

This study, while informative, is limited by several factors. First, only a limited number of load cycles are considered in the simulations. Although this provides insights into the behavior of geogrid-reinforced ballast, this may not depict the long-term response of geogrid-reinforced ballast subjected to cyclic loading. Additionally, ballast particles are represented by unbreakable mono-sized clumps. This may not represent the range of particle sizes typically encountered in railroad ballast and may not capture the breakage and degradation of ballast particles exposed to repeated loading. It is also important to note that the results presented herein are affected by choosing the linear contact model to describe interactions between ballast particles. Despite its widespread use in the discrete element modeling of railroad ballast, this contact law implies a direct proportionality between the contact force and the overlap between contacting particles, which may not accurately represent the contacts between real ballast particles. It is also noteworthy that the presence of a compressible subballast/subgrade assembly under the ballast layers is simulated by assigning a specific normal contact stiffness to the ballast box's bottom wall. This may not

capture the deformations that would normally occur in the soil layers supporting a typical ballast layer, thereby constituting a simplification of reality.

Avenues for future research include using a wider range of clumps of varying sizes and shapes to simulate ballast particles so as to more accurately match the typical particle size distribution of ballast aggregate. Ballast particles may also be modeled as breakable clumps to capture the degradation and breakage of ballast aggregate during cyclic loading and determine whether the inclusion of geogrids mitigates ballast breakage. More realistic contact laws, such as the Hertz-Mindlin contact model or the conical damage model, could be used to model the constitutive behavior of railroad ballast. Additionally, a higher number of load cycles could be simulated to provide insight into the long-term behavior of geogrid-reinforced ballast.

## 8 Conclusions

This paper presents the findings of three-dimensional discrete element simulations of ballast box tests to examine the deformation behavior of geogrid-reinforced ballast subjected to cyclic loading. The study includes a parametric study that explores the effect of the geogrid's placement depth,  $A/D$  ratio, and stiffness on the response of geogrids embedded in ballast. Results are analyzed by initially studying the macroscale behavior of reinforced ballast assemblies through the evolution of the tie's settlement during cyclic loading. The analysis then delves into the microscale processes, such as particle motion, formation of contact force chains, and energy dissipation, that contribute to the observed macroscale response to cyclic loading. The key highlights of this study are as follows:

- The tie settlement is highly sensitive to the geogrid placement depth, with geogrids situated 50 to 150 mm below the tie resulting in the most significant reductions in tie subsidence compared with the unreinforced ballast layer. The reinforcing efficiency of geogrids wanes at greater depths, leading to less pronounced reductions in tie settlement.
- The superior performance of geogrids located 50 to 150 mm beneath the tie is attributed to the formation of a robust geogrid-ballast interlock that confines the granular material. This translates into smaller particle movement developing in the granular assembly following the application of cyclic loading which considerably decreases the cumulative energy dissipated through interparticle frictional sliding. The inclusion of geogrids leads to ballast layers being better connected as evidenced by geogrid-reinforced ballast beds possessing greater coordination numbers than in the unreinforced case.
- The aperture size of a geogrid is a critical factor in the reinforcement of ballast. The parametric study indicates that an  $A/D$  ratio of 1.09 is ineffective. Its use leads to increased particle movement in the ballast layer and a corresponding increase in tie settlement. In contrast,  $A/D$  ratios equal to or greater than 1.45 are found to yield optimal reinforcement.

- Variations in geogrid stiffness caused by temperatures ranging from  $-30$  to  $40$  °C have a negligible influence on the performance of geogrid-reinforced ballast with similar tie settlements being observed across the range of geogrid stiffnesses considered in this paper.

**Acknowledgements** The first author is grateful for the technical advice provided by Prof. Ge Gao from Shanghai Jiao Tong University.

**Author Contribution** RLED: conceptualization, methodology, investigation, formal analysis, visualization, resources, writing—original draft. MAM: funding acquisition, resources, supervision, writing—review and editing. SB: funding acquisition, writing—review and editing.

**Funding** This research is funded by an NSERC Alliance grant (NSERC ALLRP 5617) in partnership with Titan Environmental Ltd. and by the McGill Engineering Vadasz Doctoral Fellowship sponsored by the Vadasz Family Foundation.

**Data Availability** The data supporting the findings of this study are available upon reasonable request from the corresponding author.

## Declarations

**Competing Interests** The authors declare no competing interests.

## References

- Alabbasi, Y., Hussein, M.: Geomechanical modelling of railroad ballast: a review. *Arch Comput Methods Eng* **28**(3), 815–839 (2021). <https://doi.org/10.1007/s11831-019-09390-4>
- AREMA.: *Manual for railway engineering*. American Railway Engineering and Maintenance-of-Way Association, Lanham (2010)
- Bathurst, R.J., Raymond, G.P.: Geogrid reinforcement of ballasted track. *Transp Research Rec* **1153**, 8–14 (1987)
- Bathurst, R.J., Raymond, G.P., Jarrett, P.M.: Performance of geogrid-reinforced ballast railroad track support. *Third Int Conf Geotextiles* **80**, 43–48 (1986)
- Bian, X., Li, W., Qian, Y., Tutumluer, E.: Analysing the effect of principal stress rotation on railway track settlement by discrete element method. *Geotechnique* **70**(9), 803–821 (2020). <https://doi.org/10.1680/jgeot.18.P.368>
- Brown, S.F., Kwan, J., Thom, N.H.: Identifying the key parameters that influence geogrid reinforcement of railway ballast. *Geotextiles Geomembr* **25**(6), 326–335 (2007). <https://doi.org/10.1016/j.geotexmem.2007.06.003>
- Chen, C., McDowell, G.R., Thom, N.H.: Discrete element modelling of cyclic loads of geogrid-reinforced ballast under confined and unconfined conditions. *Geotextiles Geomembr* **35**, 76–86 (2012). <https://doi.org/10.1016/j.geotexmem.2012.07.004>
- Chen, C., McDowell, G.R., Thom, N.H.: A study of geogrid-reinforced ballast using laboratory pull-out tests and discrete element modelling. *Geomech Geoeng* **8**(4), 244–253 (2013). <https://doi.org/10.1080/17486025.2013.805253>
- Chen, C., McDowell, G.R., Thom, N.H.: Investigating geogrid-reinforced ballast: experimental pull-out tests and discrete element modelling. *Soils Found* **54**(1), 1–11 (2014). <https://doi.org/10.1016/j.sandf.2013.12.001>
- Chen, C., Indraratna, B., McDowell, G., Rujikiatkamjorn, C.: Discrete element modelling of lateral displacement of a granular assembly under cyclic loading. *Comp Geotechnics* **69**, 474–484 (2015). <https://doi.org/10.1016/j.compgeo.2015.06.006>

- Chen, J., Bao, N., Sun, R.: Three-dimensional discrete-element-method analysis of behavior of geogrid-reinforced sand foundations under strip footing. *Int J Geomech* **22**(9), 1–16 (2022a). [https://doi.org/10.1061/\(asce\)gm.1943-5622.0002543](https://doi.org/10.1061/(asce)gm.1943-5622.0002543)
- Chen, W., Zhang, Y., Wang, C., Xiao, Y., Lou, P.: Effect of ballast pockets and geogrid reinforcement on ballasted track: numerical analysis. *Transportation Geotechnics* **42**, 101108 (2023). <https://doi.org/10.1016/j.trgeo.2023.101108>
- Chen, J., Vinod, J. S., Indraratna, B., Ngo, N. T., Gao, R., Liu, Y.: A discrete element study on the deformation and degradation of coal-fouled ballast. *Acta Geotechnica*, 4. (2022b). <https://doi.org/10.1007/s11440-022-01453-4>
- D'Angelo, G., Sol-Sanchez, M., Moreno-Navarro, F., Lo Presti, D., Thom, N.: Use of bitumen-stabilised ballast for improving railway trackbed conventional maintenance. *Geotechnique* **68**(6), 518–527 (2018). <https://doi.org/10.1680/jgeot.17.P.022>
- Dahlberg, T.: Some railroad settlement models—a critical review. *Proc Inst Mech Eng, Part F: J Rail Rapid Transit* **215**(4), 289–300 (2001). <https://doi.org/10.1243/0954409011531585>
- Das, B.M.: Use of geogrid in the construction of railroads. *Innov Infrastruct Solutions* **1**(1), 15 (2016). <https://doi.org/10.1007/s41062-016-0017-8>
- Desbrousses, R.L.E., Meguid, M.A.: On the analysis and design of reinforced railway embankments in cold climate: a review. In: Tighe, S., Walbridge, S., Henderson, V. (eds.) *CSCCE 2021 Annual Conference*, pp. 588–598. Springer (2021)
- Desbrousses, R.L.E., Meguid, M.A., Bhat, S.: Experimental investigation of the effects of subgrade strength and geogrid location on the cyclic response of geogrid-reinforced ballast. *Int J Geosynth Ground Eng* **9**(6), 67 (2023). <https://doi.org/10.1007/s40891-023-00486-3>
- Desbrousses, R.L.E., Meguid, M.A.: Effect of subgrade compressibility on the reinforcing performance of railroad geogrids: insights from finite element analysis. In: *Canadian Geotechnical Society (eds.) GeoCalgary. Canadian Geotechnical Society, Calgary* (2022)
- Desbrousses, R. L. E., & Meguid, M. A.: Geogrids in cold climates: insights from in-isolation tensile tests at low temperatures. In *Geosynthetics: Leading the Way to a Resilient Planet* (pp. 467–473). CRC Press. (2023a). <https://doi.org/10.1201/9781003386889-45>
- Desbrousses, R.L.E., Meguid, M.A.: On the design of a pneumatic cyclic loading setup for geotechnical testing. In: *C. G. Society (ed.) GeoSaskatoon 2023. Canadian Geotechnical Society* (2023b)
- Desbrousses, R. L. E., Meguid, M. A., Bhat, S.: Effect of temperature on the mechanical properties of two polymeric geogrid materials. *Geosynthetics International*, 1–31. (2021). <https://doi.org/10.1680/jgein.21.00032a>
- Desbrousses, R.L.E., Meguid, M.A., Bhat, S.: On the effect of subgrade strength on the performance of geogrid-reinforced ballast. *GeoAmericas, Toronto* (2024)
- Esmaili, M., Zakeri, J.A., Babaei, M.: Laboratory and field investigation of the effect of geogrid-reinforced ballast on railway track lateral resistance. *Geotextiles Geomembr* **45**(2), 23–33 (2017). <https://doi.org/10.1016/j.geotextmem.2016.11.003>
- Fei, W., Narsilio, G.A.: Impact of three-dimensional sphericity and roundness on coordination number. *J Geotech Geoenviron Eng* **146**(12), 1–7 (2020). [https://doi.org/10.1061/\(asce\)gt.1943-5606.0002389](https://doi.org/10.1061/(asce)gt.1943-5606.0002389)
- Feng, S. J., & Wang, Y. Q. (2023). DEM simulation of geogrid–aggregate interface shear behavior: optimization of the aperture ratio considering the initial interlocking states. *Computers and Geotechnics*, 154(December 2022), 105182. (2023). <https://doi.org/10.1016/j.compgeo.2022.105182>
- Ferrellec, J.-F., McDowell, G.R.: Modelling of ballast–geogrid interaction using the discrete-element method. *Geosynth Int* **19**(6), 470–479 (2012). <https://doi.org/10.1680/gein.12.00031>
- Fernandes, G., Palmeira, E.M., Gomes, R.C.: Performance of geosynthetic-reinforced alternative sub-ballast material in a railway track. *Geosynth Int* **15**(5), 311–321 (2008). <https://doi.org/10.1680/gein.2008.15.5.311>
- Gao, G., Meguid, M.A.: Effect of particle shape on the response of geogrid-reinforced systems: insights from 3D discrete element analysis. *Geotextiles Geomembr* **46**(6), 685–698 (2018). <https://doi.org/10.1016/j.geotextmem.2018.07.001>
- Gu, X., Huang, M., Qian, J.: DEM investigation on the evolution of microstructure in granular soils under shearing. *Granular Matter* **16**(1), 91–106 (2014). <https://doi.org/10.1007/s10035-013-0467-z>
- Guo, Y., Zhao, C., Markine, V., Shi, C., Jing, G., Zhai, W.: Discrete element modelling of railway ballast performance considering particle shape and rolling resistance. *Railway Eng Sci* **28**(4), 382–407 (2020). <https://doi.org/10.1007/s40534-020-00216-9>
- Guo, Y., Markine, V., Jing, G.: Review of ballast track tamping: mechanism, challenges and solutions. *Construct Build Mater* **300**, 123940 (2021). <https://doi.org/10.1016/j.conbuildmat.2021.123940>

- Han, J., Bhandari, A., Wang, F.: DEM analysis of stresses and deformations of geogrid-reinforced embankments over piles. *Int J Geomech* **12**(4), 340–350 (2012). [https://doi.org/10.1061/\(asce\)gm.1943-5622.0000050](https://doi.org/10.1061/(asce)gm.1943-5622.0000050)
- Hussaini, S.K.K., Sweta, K.: Application of geogrids in stabilizing rail track substructure. *Front Built Environ* **6**(February), 1–13 (2020). <https://doi.org/10.3389/fbuil.2020.00020>
- Hussaini, S.K.K., Sweta, K.: Investigation of deformation and degradation response of geogrid-reinforced ballast based on model track tests. *Proc Inst Mech Eng, Part F: J Rail Rapid Transit* **235**(4), 505–517 (2021). <https://doi.org/10.1177/0954409720944687>
- Hussaini, S.K.K., Indraratna, B., Vinod, J.S.: Performance assessment of geogrid-reinforced railroad ballast during cyclic loading. *Transportation Geotechnics* **2**, 99–107 (2015). <https://doi.org/10.1016/j.trgeo.2014.11.002>
- Hussaini, S.K.K., Indraratna, B., Vinod, J.S.: A laboratory investigation to assess the functioning of railway ballast with and without geogrids. *Transp Geotech* **6**, 45–54 (2016). <https://doi.org/10.1016/j.trgeo.2016.02.001>
- Indraratna, B., Lackenby, J., Christie, D.: Effect of confining pressure on the degradation of ballast under cyclic loading. *Géotechnique* **55**(4), 325–328 (2005). <https://doi.org/10.1680/geot.2005.55.4.325>
- Indraratna, B., Nimbalkar, S., Christie, D., Rujikiatkamjorn, C., Vinod, J.: Field assessment of the performance of a ballasted rail track with and without geosynthetics. *J Geotech Geoenviron Eng* **136**(7), 907–917 (2010). [https://doi.org/10.1061/\(ASCE\)GT.1943-5606.0000312](https://doi.org/10.1061/(ASCE)GT.1943-5606.0000312)
- Indraratna, B., Ngo, N.T., Rujikiatkamjorn, C.: Behavior of geogrid-reinforced ballast under various levels of fouling. *Geotextiles Geomembr* **29**(3), 313–322 (2011). <https://doi.org/10.1016/j.geotexmem.2011.01.015>
- Indraratna, B., Karimullah Hussaini, Sd.K., Vinod, J.S.: On the shear behavior of ballast-geosynthetic interfaces. *Geotech Test J* **35**(2), 103317 (2012). <https://doi.org/10.1520/GTJ103317>
- Indraratna, B., Hussaini, S.K.K., Vinod, J.S.: The lateral displacement response of geogrid-reinforced ballast under cyclic loading. *Geotextiles Geomembr* **39**, 20–29 (2013). <https://doi.org/10.1016/j.geotexmem.2013.07.007>
- Indraratna, B., Ngo, T., Bessa Ferreira, F., Rujikiatkamjorn, C., Shahkolahi, A.: Laboratory examination of ballast deformation and degradation under impact loads with synthetic inclusions. *Transportation Geotechnics* **25**, 100406 (2020). <https://doi.org/10.1016/j.trgeo.2020.100406>
- Itasca Consulting Group Inc.: Pavement Design Package for PFC3D. Itasca Consulting Group Inc. (2019). <https://www.itasca.ca/software/pavement-design-package-in-pfc>
- Itasca: Particle Flow Code 3D (Version 7.0) [Computer software]. Itasca Consulting Group Inc. (2022). <https://www.itasca.ca/software/pfc>
- Jiang, Y., Nimbalkar, S.: Finite element modeling of ballasted rail track capturing effects of geosynthetic inclusions. *Front Built Environ* **5**(May), 1–11 (2019). <https://doi.org/10.3389/fbuil.2019.00069>
- Kumar, N., Stühr, B., Marschnig, S., Dietmaier, P., Marte, C., Six, K.: Micro-mechanical investigation of railway ballast behavior under cyclic loading in a box test using DEM: effects of elastic layers and ballast types. *Granular Matter* **21**(4), 1–17 (2019). <https://doi.org/10.1007/s10035-019-0956-9>
- Lackenby, J., Indraratna, B., McDowell, G., Christie, D.: Effect of confining pressure on ballast degradation and deformation under cyclic triaxial loading. *Géotechnique* **57**(6), 527–536 (2007). <https://doi.org/10.1680/geot.2007.57.6.527>
- Lai, H.J., Zheng, J.J., Zhang, J., Zhang, R.J., Cui, L.: DEM analysis of “soil”-arching within geogrid-reinforced and unreinforced pile-supported embankments. *Comp Geotech* **61**, 13–23 (2014). <https://doi.org/10.1016/j.compgeo.2014.04.007>
- Li, H., McDowell, G.R.: Discrete element modelling of under sleeper pads using a box test. *Granular Matter* **20**(2), 1–12 (2018). <https://doi.org/10.1007/s10035-018-0795-0>
- Li, H., McDowell, G.: Discrete element modelling of two-layered ballast in a box test. *Granular Matter* **22**(4), 1–14 (2020). <https://doi.org/10.1007/s10035-020-01046-6>
- Li, D., Hyslip, J., Sussmann, T., Chrismer, S.: *Railway Geotechnics*. CRC Press (2015). <https://doi.org/10.1201/b18982>
- Li, C., Gao, R., Hu, Q., Chen, J.: Effect of the combination of geogrid and rubber granules on the performance of ballast under impact loads. *Granular Matter* **26**(1), 10 (2024). <https://doi.org/10.1007/s10035-023-01384-1>
- Lim, W.L., McDowell, G.R.: Discrete element modelling of railway ballast. *Granular Matter* **7**(1), 19–29 (2005). <https://doi.org/10.1007/s10035-004-0189-3>



- Liu, S., Huang, H., Qiu, T., Kwon, J.: Effect of geogrid on railroad ballast particle movement. *Transp Geotech* **9**, 110–122 (2016). <https://doi.org/10.1016/j.trgeo.2016.08.003>
- Liu, J., Zhou, W., Ma, G., Yang, S., Chang, X.: Strong contacts, connectivity and fabric anisotropy in granular materials: a 3D perspective. *Powder Technol* **366**, 747–760 (2020). <https://doi.org/10.1016/j.powtec.2020.03.018>
- Liu, Y., & Yan, Z.: Study on strong contact system by sub-network partitioning method for binary mixtures. *European Journal of Environmental and Civil Engineering*, 1–25. (2023). <https://doi.org/10.1080/19648189.2023.2268691>
- Luo, Z., Zhao, C., Bian, X., Chen, Y.: Discrete element analysis of geogrid-stabilized ballasted tracks under high-speed train moving loads. *Comp Geotech* **159**(March), 105451 (2023a). <https://doi.org/10.1016/j.compgeo.2023.105451>
- Luo, Z., Zhao, C., Cai, W., Gu, Q., Lin, W., Bian, X., & Chen, Y.: Full-scale model tests on ballasted tracks with/without geogrid-stabilization under high-speed train loads. *Geotechnique*, 1–15. (2023b). <https://doi.org/10.1680/jgeot.22.00339>
- Malisetty, R. S., Indraratna, B., Qi, Y., & Rujikiatkamjorn, C.: Shakedown response of recycled rubber-granular waste mixtures under cyclic loading. *Geotechnique*, 1. (2022). <https://doi.org/10.1680/jgeot.21.00040>
- McDowell, G.R., Stickley, P.: Performance of geogrid-reinforced ballast. *Ground Eng* **39**(1), 26–30 (2006)
- McDowell, G.R., Harireche, O., Konietzky, H., Brown, S.F., Thom, N.H.: Discrete element modelling of geogrid-reinforced aggregates. *Proc Inst Civil Eng - Geotech Eng* **159**(1), 35–48 (2006). <https://doi.org/10.1680/geng.2006.159.1.35>
- Minh, N.H., Cheng, Y.P.: A DEM investigation of the effect of particle-size distribution on one-dimensional compression. *Geotechnique* **63**(1), 44–53 (2013). <https://doi.org/10.1680/geot.10.P.058>
- Minh, N.H., Cheng, Y.P., Thornton, C.: Strong force networks in granular mixtures. *Granular Matter* **16**(1), 69–78 (2014). <https://doi.org/10.1007/s10035-013-0455-3>
- Mishra, D., Qian, Y., Kazmee, H., Tutumluer, E.: Investigation of geogrid-reinforced railroad ballast behavior using large-scale triaxial testing and discrete element modeling. *Transp Res Rec: J Transp Res Board* **2462**(1), 98–108 (2014). <https://doi.org/10.3141/2462-12>
- Ngo, N.T., Indraratna, B.: Improved performance of rail track substructure using synthetic inclusions: experimental and numerical investigations. *Int J Geosynth Ground Eng* **2**(3), 1–16 (2016). <https://doi.org/10.1007/s40891-016-0065-3>
- Ngo, N.T., Indraratna, B., Rujikiatkamjorn, C.: DEM simulation of the behaviour of geogrid stabilised ballast fouled with coal. *Comp Geotech* **55**, 224–231 (2014). <https://doi.org/10.1016/j.compgeo.2013.09.008>
- O'Sullivan, C.: Particulate discrete element modelling. In *Particulate Discrete Element Modelling*. (2011). <https://doi.org/10.1201/9781482266498>
- Offenbacher, S., Antony, B., Barbir, O., Auer, F., Landgraf, M.: Evaluating the applicability of multi-sensor equipped tamping machines for ballast condition monitoring. *Measurement* **172**, 108881 (2021). <https://doi.org/10.1016/j.measurement.2020.108881>
- Oudfel, H.: Numerical simulations of granular assemblies with three-dimensional ellipsoid-shaped particles [Doctoral dissertation, University of Waterloo]. University of Waterloo's Institutional Repository (1998). <https://uwspace.uwaterloo.ca/handle/10012/331>
- Qian, Y., Mishra, D., Tutumluer, E., Kazmee, H.A.: Characterization of geogrid reinforced ballast behavior at different levels of degradation through triaxial shear strength test and discrete element modeling. *Geotextiles Geomembr* **43**(5), 393–402 (2015). <https://doi.org/10.1016/j.geotextmem.2015.04.012>
- Qian, Y., Tutumluer, E., Mishra, D., Kazmee, H.: Triaxial testing and discrete-element modelling of geogrid-stabilised rail ballast. *Proc Inst Civil Eng: Ground Improv* **171**(4), 223–231 (2018). <https://doi.org/10.1680/jgrim.17.00068>
- Radjai, F., Wolf, D.E., Jean, M., Moreau, J.-J.: Bimodal character of stress transmission in granular packings. *Phys Rev Lett* **80**(1), 61–64 (1998). <https://doi.org/10.1103/PhysRevLett.80.61>
- Radjai, F., Wolf, D.E., Roux, S., Jean, M., Moreau, J.J.: Force networks in dense granular media. *Powders and grains*, Durham, pp. 211–214 (1997)
- Sadeghi, J., Tolou Kian, A.R., Ghiasinejad, H., Fallah Moqaddam, M., Motevalli, S.: Effectiveness of geogrid reinforcement in improvement of mechanical behavior of sand-contaminated ballast. *Geotextiles Geomembr* **48**(6), 768–779 (2020). <https://doi.org/10.1016/j.geotextmem.2020.05.007>

- Sadeghi, J., Tolou Kian, A. R., Khanmoradi, A., & Chopani, M.: Behavior of sand-contaminated ballast reinforced with geogrid under cyclic loading. *Construction and Building Materials*, 362(August 2022), 129654. (2023). <https://doi.org/10.1016/j.conbuildmat.2022.129654>
- Selig, E. T., Waters, J. M.: Track geotechnology and substructure management. Thomas Telford Publications, London (1994). <https://doi.org/10.1680/tgasm.20139>
- Shi, S., Gao, L., Cai, X., Xiao, Y., Xu, M.: Mechanical characteristics of ballasted track under different tamping depths in railway maintenance. *Transportation Geotechnics* 35, 100799 (2022). <https://doi.org/10.1016/j.trgeo.2022.100799>
- Shi, D., Niu, J., Zhang, J., Chao, Z., & Fowmes, G.: Effects of particle breakage on the mechanical characteristics of geogrid-reinforced granular soils under triaxial shear: a DEM investigation. *Geomechanics for Energy and the Environment*, 34. (2023). <https://doi.org/10.1016/j.gete.2023.100446>
- Shin, E.C., Das, B.M.: Experimental study of bearing capacity of a strip foundation on geogrid-reinforced sand. *Geosynth Int* 7(1), 59–71 (2000). <https://doi.org/10.1680/gein.7.0166>
- Shin, E.C., Kim, D.H., Das, B.M.: Geogrid-reinforced railroad bed settlement due to cyclic load. *Geotech Geol Eng* 20(3), 261–271 (2002). <https://doi.org/10.1023/A:1016040414725>
- Stahl, M., Konietzky, H., te Kamp, L., Jas, H.: Discrete element simulation of geogrid-stabilised soil. *Acta Geotechnica* 9(6), 1073–1084 (2014). <https://doi.org/10.1007/s11440-013-0265-0>
- Suhr, B., Six, K.: Parametrisation of a DEM model for railway ballast under different load cases. *Granular Matter* 19(4), 1–16 (2017). <https://doi.org/10.1007/s10035-017-0740-7>
- Suhr, B., Six, K.: Simple particle shapes for DEM simulations of railway ballast: influence of shape descriptors on packing behaviour. *Granular Matter* 22(2), 1–17 (2020). <https://doi.org/10.1007/s10035-020-1009-0>
- Suhr, B., Six, K.: Efficient DEM simulations of railway ballast using simple particle shapes. *Granular Matter* 24(4), 1–19 (2022). <https://doi.org/10.1007/s10035-022-01274-y>
- Suiker, A.S.J., Selig, E.T., Frenkel, R.: Static and cyclic triaxial testing of ballast and subballast. *J Geotech Geoenviron Eng* 131(6), 771–782 (2005). [https://doi.org/10.1061/\(ASCE\)1090-0241\(2005\)131:6\(771\)](https://doi.org/10.1061/(ASCE)1090-0241(2005)131:6(771))
- Sweta, K., Hussaini, S.K.K.: Effect of shearing rate on the behavior of geogrid-reinforced railroad ballast under direct shear conditions. *Geotextiles Geomembr* 46(3), 251–256 (2018). <https://doi.org/10.1016/j.geotextmem.2017.12.001>
- Sweta, K., Hussaini, S.K.K.: Behavior evaluation of geogrid-reinforced ballast-subballast interface under shear condition. *Geotextiles Geomembr* 47(1), 23–31 (2019). <https://doi.org/10.1016/j.geotextmem.2018.09.002>
- Sweta, K., Hussaini, S.K.K.: Effect of geogrid on deformation response and resilient modulus of railroad ballast under cyclic loading. *Const Buil Mater* 264, 120690 (2020). <https://doi.org/10.1016/j.conbuildmat.2020.120690>
- Sweta, K., Hussaini, S.K.K.: Role of particle breakage on damping, resiliency and service life of geogrid-reinforced ballasted tracks. *Transp Geotech* 37(July), 100828 (2022). <https://doi.org/10.1016/j.trgeo.2022.100828>
- Thakur, P.K., Vinod, J.S., Indraratna, B.: Effect of confining pressure and frequency on the deformation of ballast. *Geotechnique* 63(9), 786–790 (2013). <https://doi.org/10.1680/geot.12.T.001>
- Thornton, C., Antony, S.J.: Quasi-static deformation of particulate media philosophical transactions of the royal Society of London. Series A: Math, Phys Eng Sci 356(1747), 2763–2782 (1998). <https://doi.org/10.1098/rsta.1998.0296>
- Titan Environmental Containment.: Titan Rail Grid 30 (2023). <https://titanenviro.com/wp-content/uploads/2023/09/Titan-Rail-Grid-30.pdf>
- Tolomeo, M., McDowell, G.R.: Modelling real particle shape in DEM: a comparison of two methods with application to railway ballast. *Int J Rock Mech Mining Sci* 159(December 2021), 105221 (2022). <https://doi.org/10.1016/j.ijrmm.2022.105221>
- Tutumluer, E., Huang, H., Bian, X.: Geogrid-aggregate interlock mechanism investigated through aggregate imaging-based discrete element modeling approach. *I J Geomech* 12(4), 391–398 (2012). [https://doi.org/10.1061/\(ASCE\)GM.1943-5622.0000113](https://doi.org/10.1061/(ASCE)GM.1943-5622.0000113)
- Wang, K., Zhuang, Y., Kouretzis, G., Sloan, S.W.: Shakedown analysis of ballasted track structure using three-dimensional finite element techniques. *Acta Geotechnica* 15(5), 1231–1241 (2020). <https://doi.org/10.1007/s11440-019-00818-6>

- Wang, Y.-Q., Feng, S.-J., Zhao, Y., Zheng, Q.-T.: Microscale analysis of geogrid–aggregate interface cyclic shear behavior using DEM. *Comp Geotech* **166**, 105973 (2024). <https://doi.org/10.1016/j.compgeo.2023.105973>
- Yu, Z., Woodward, P.K., Laghrouche, O., Connolly, D.P.: True triaxial testing of geogrid for high speed railways. *Transp Geotech* **20**(May), 100247 (2019). <https://doi.org/10.1016/j.trgeo.2019.100247>
- Zhang, F., Yao, Q., Wang, H., Feng, H., Chang, J., Lu, L., Yue, Z., Jiang, M.: DEM analysis of the cyclic behavior of ballast mixed with crumb rubber. *Construct Build Mater* **375**(March), 130975 (2023). <https://doi.org/10.1016/j.conbuildmat.2023.130975>

**Publisher's Note** Springer Nature remains neutral with regard to jurisdictional claims in published maps and institutional affiliations.

Springer Nature or its licensor (e.g. a society or other partner) holds exclusive rights to this article under a publishing agreement with the author(s) or other rightsholder(s); author self-archiving of the accepted manuscript version of this article is solely governed by the terms of such publishing agreement and applicable law.

## Authors and Affiliations

Romarc Léo Esteban Desbrousses<sup>1</sup> · Mohamed A. Meguid<sup>1</sup> · Sam Bhat<sup>2</sup>

✉ Romarc Léo Esteban Desbrousses  
romarc.desbrousses@mail.mcgill.ca

Mohamed A. Meguid  
mohamed.meguid@mcgill.ca

Sam Bhat  
sam@titanenviro.ca

<sup>1</sup> Department of Civil Engineering, McGill University, 817 Sherbrooke St. W, Montreal, QC H3A 0C3, Canada

<sup>2</sup> Titan Environmental Containment Ltd, 777 Quest Blvd, Ile des Chenes, Manitoba R0A 0T1, Canada